Norwegian University
of Life Sciences

Master's Thesis 2017 60 ECTS
Faculty of Technology and Science

The Structuring of High Latitude Aurora

Natalie Forseth
Miljøfysikk

Acknowledgements

I am just realizing that my arctic adventure is coming to an end and I can only conclude that this year has been amazing. I have learned a lot about science, about myself, but most importantly that I would like to pursue a career in scientific research. Writing this thesis is my greatest achievement so far and I would like to acknowledge everyone who helped on the road.

I want to begin with expressing my deepest gratitude to my main supervisor Dr. Lisa Baddeley for excellent guidance, patience and motivation throughout this past year. Your door has always been open whenever I had questions or just needed a discussion. Thanks for being nice when I though I was going to loose my mind.
I would like to show my greatest appreciation to my associate supervisor Arne Auen Grimenes for all help not only with this thesis, but also with coordinating everything with my home institution, NMBU. Your enthusiasm and encouragement have been truly inspirational ever since my first year as a Bachelor student.
I would like to offer my special thanks to my associate supervisor Dr. Noora Partamies for exemplary guidance, motivation, feedback and also providing me with the data for this project.
My stay at UNIS would not have been the same without the wonderful students and staff surrounding me every day. I am forever thankful to my office mates at the Department of Geophysics at UNIS: Markus Richter, Léa Olivier and Karl Bolmgren for their friendship, discussions, cakes and creating a pleasant working environment. I would also like to thank Magnus Isaksen for all help with MATLAB and LaTeX, and being my best friend.

Obtaining the degree as Master of Science has not only been about the year writing the thesis, but about the journey getting there. I owe a very

important debt to my high school physics teacher, Sophie Cordon, for inspiring me to pursue studies in physics and introducing me to Svalbard. Without that, I would probably not have discovered the field of Space Physics.
I would like to thank 4DSpace and the Space-and Plasma Physics group at the University of Oslo for including me in their research group. I also want to thank Dr. Kathryn McWilliams at the University of Saskatchewan for having me as a summer student which permitted me to gain the knowledge I wanted in SuperDARN radars.

Finally, my deep and sincere gratitude to my family and friends for always being helpful and supporting, no matter what.

Longyearbyen, May 2017

Natalie Forseth

Abstract

The interaction between the Earths magnetic field and interplanetary magnetic field (IMF), originating from the Sun, is the driving force behind the aurora. Due to the phenomena of polar night, the optical signatures of dayside aurora can be investigated over Svalbard. In order to ease the examination of All-sky camera (ASC) images, an algorithm is used to quantify the observed auroral forms in terms of an "arciness" index (A, ranging from 0 to 1) describing how arc-like the shape of the green emission lines (557.7 nm) in the image is. This algorithm was applied to ASC images from Longyearbyen and Ny-Ålesund between 2000 and 2012, in combination with solar wind parameters (IMF B_z and B_y components and solar wind velocity) to obtain a general temporal distribution of dayside auroral structures. The temporal distribution as well as the arciness index permits the identification of the type of dayside aurora and their originating precipitation region. The analysis has been done for both polarities of IMF B_z, taking into account the contribution from the IMF B_y component. Auroral types, earlier defined by Sandholt et al.(2002), were identified by their corresponding arciness: arcs (A=1) or complex structures (A<0.9), their location throughout the day and also their latitudinal location. The effects of the solar wind velocity on the arciness has also been discussed revealing no clear correlation. For weak solar wind velocities (v<400 km/s), a recurring temporal distribution of both arcs (A=1) and complex auroral structures (A<0.9) in the mid-morning sector (09.00-11.00 MLT) was observed and related to cusp auroras and multiple morning arcs. The arciness index permits a simple identification of arc-like auroral forms in the green emission band observed in previous studies. However it does not cover the red emission line (630.0 nm) which is often present in the cusp region. Also, auroral structures not shaped like arcs are challenging to recognize.

Contents

Abbreviations and Acronyms

ACE	Advanced Composition Explorer
ASC	All-Sky Camera
BJN	Bjørnøya
BPS	Boundary Plasma Sheet
CCD	Charged Coupled Device
CME	Coronal Mass Ejections
CPS	Central Plasma Sheet
FAC	Field Aligned Current
FMI	Finnish Meteorological Institute
GPS	Global Positioning System
HCS	Heliospheric Current Sheet
HOP	Hopen
HOR	Hornsund
ICME	Interplanetary Coronal Mass Ejections
IMF	Interplanetary Magnetic Field
KHO	Kjell Henriksen Observatory
LLBL	Low-Latitude Boundary Layer
LYR	Longyearbyen
MHD	Magnetohydrodynamics

MIRACLE	Magnetometers Ionospheric Radars All-sky Cameras Large Experiment
MLAT	Magnetic Latitude
MLT	Magnetic Local Time
NAL	Ny-Ålesund
NMBU	Norwegian University of Life Sciences
OCB	Open-closed Magnetic Field Line Boundary
OI	Atomic oxygen
PMAF	Poleward Moving Auroral Forms
SBC	Sector Boundary Crossings
UNIS	University Centre in Svalbard
UT	Universal Time
UV	Ultraviolet

Chapter 1

Introduction

For thousands of years, people have been fascinated by the light dancing over the night sky in the polar regions. Galileo Galilei named them "Aurora" in 1610 A.D. after the Roman goddess of morning, as he believed the auroras were caused by the reflection of sunlight in the atmosphere. The aurora arises from the coupling between the interplanetary magnetic field (IMF), carried by the solar wind, and the geomagnetic field. Particles originating from the Sun will be guided into the Earth's upper atmosphere and then collide with the atmospheric particles producing auroral emissions.

One way to record and observe the visible mesoscale aurora (10-100km) is by All-Sky Cameras (ASC) and then investigate the data sets in case studies. Clouds and light pollution can often interfere with the data and therefore a visual inspection of the images is usually necessary. For large data sets, visual inspection is time consuming and may introduce a human bias. To conduct a statistical study of trends in the aurora, an algorithm has been developed to easily quantify the auroral structures in large data sets by means of the "arciness" index [Partamies et al., 2014]. This algorithm has been used for statistical studies, of 11 years of ASC data from Northern Sweden and Northern Finland where the nightside aurora was correlated to geomagnetic activity and diurnal and seasonal variations.

This thesis will, for the first time, attempt to statistically identify the structuring of the dayside aurora using a numerical, as opposed to a descriptive scale, utilizing ASC data from two stations on Svalbard: Longyearbyen and Ny-Ålesund. The high latitude position of Svalbard makes it possible to observe the dayside aurora due to the polar night when the Sun is below the horizon and permit the study of the cusp and dayside auroral region using optical instrumentation.

The data set consists of 13 years of arciness and solar wind data from 2000 to 2012. The time distribution of the arciness index, depending on IMF B_z and B_y components as well as the solar wind velocity, has been studied in order to identify the dayside auroral forms in comparison with observations made by Sandholt et al.(2002).

This analysis will investigate the distribution of dayside auroral forms in terms of arciness index for northward and southward oriented IMF B_z separately as they result from different reconnection mechanisms: tail lobe reconnection and magnetopause reconnection, respectively. For both orientations of the IMF B_z, the polarities of the B_y component have been considered, as their contribution changes the reconnection geometry towards dusk or dawn creating different directed movements of the auroral forms. The impact of the strength of solar wind velocity on the arciness, hence, on the dayside auroral forms has also been looked into.

Chapter 2

Background

2.1 The Solar Wind

2.1.1 Expulsion of the Solar Wind

Space weather begins with releasing of material from the solar surface that will travel through the heliosphere and interact with the terrestrial environment.

Heat from the innermost layers of the Sun is transported out to the solar atmosphere by radiation and convection. Photons and energetic particles from the inner layers get absorbed by the layers on top of them which again will be absorbed and emitted by the layer above and the radiative energy is then transported out to the Sun's atmosphere [Brekke, 2013]. The solar atmosphere is organized in three main regions: photosphere, chromosphere and corona.

At the solar surface, sunspots appear as darker areas because they are colder than the their surroundings. The magnetic solar activity vary in 11-year cycles (one solar cycle is 11 years). The population (sunspot number) as well as the sunspot position vary with the phases of the solar cycle. Powerful currents in the Sun's convection zone generate strong magnetic fields that rise slowly, bringing the the Sun's magnetic field lines to the surface at the sunspots [Lepping et al., 2003].

Continuous ejections of ionized plasma from the Sun are defined as "solar wind" [E.Parker, 1959]. The solar wind is characterized as fast when its velocity reaches 850 km/s, or slow for velocities around 400 km/s, depending on the solar mechanism that expels it. Coronal holes are darker areas of the corona with lower temperatures as well as lower energy and gas levels which will result in a low density plasma in these

regions. This decrease in temperature and density is causing a thin surface which will make it easier for particles from the chromosphere to drift along the magnetic field lines that are open in the coronal holes. The fast solar wind will then escape through these corona holes [Kivelson and Russel, 1995]. Depending on the phase of the solar cycle, the amount of "helmet streamers" (loops of closed magnetic field lines around the Sun's equatorial belt) on the solar surface will vary [Lepping et al., 2003]. They are reconnected magnetic field lines extending outwards and are believed to be the source of the slow solar wind [Lepping et al., 2003].

The interplay between the coronal magnetic field and its expansion produces a structured corona and a spatially variable solar wind [Gosling and Pizzo, 1999]. The physical explanation for the solar wind being pushed outwards from the Sun is that the pressure gradient force in the radial direction is much larger than the gravitational force in the radial direction because gravity decreases as $\frac{1}{r^2}$ and pressure as $\frac{1}{r}$ as the plasma expands radially [Kivelson and Russel, 1995, Pécseli, 2013].

If we assume the plasma to expand and only propagate in the radial direction, the equations for continuity and motion will be:

$$4\pi r^2 \rho U = constant \tag{2.1}$$

$$\rho U \frac{dU}{dr} = -\frac{dp}{dr} - \rho \frac{M_\odot G}{r^2} \tag{2.2}$$

Here, r is the radial distance, ρ is the density, U is the radial velocity of the gas, p is the pressure, $M_\odot$ is the mass of the Sun and G is the gravitational constant.

Equation 2.1, the continuity equation, states that any net mass flux through a spherical surface is constant. Equation 2.2, the momentum equation, describes the acceleration a volume element experiences in the radial direction equals the sum of all the forces acting on the volume element (the $\mathbf{J} \times \mathbf{B}$-force is ignored).

The solar wind travelling out from the Sun is transporting highly conductive plasma. The Sun's open magnetic field lines will therefore be frozen into the plasma and travel through the heliosphere as Interplanetary Magnetic Field (IMF). In figure 2.1, the IMF vector is pointing away from the Sun in the northern hemisphere and towards the Sun in the southern hemisphere. In the equatorial plane this will cause a current sheet to form as a boundary between the oppositely directed IMF vectors, the Heliospheric Current Sheet (HCS). At the end of each 11-year long solar cycle, the dipole field

changes polarity and the IMF will then be directed in opposite directions then in the previous cycle (field lines directed away from the Sun are now pointing towards and vice versa). Close the poles, coronal holes are commonly located with open solar magnetic field lines which allows the plasma to flow out more easily and expand since it is no longer controlled by the field lines. The solar wind velocity is higher over higher latitudes [Gosling and Pizzo, 1999] and varies with latitude as shown in figure 2.1. Most of the high speed solar wind maps therefore into the polar corona and the slow speed solar wind occupies a relatively thin band around the Sun's magnetic equator where the helmet streamers typically are located [Feldman, 1999].

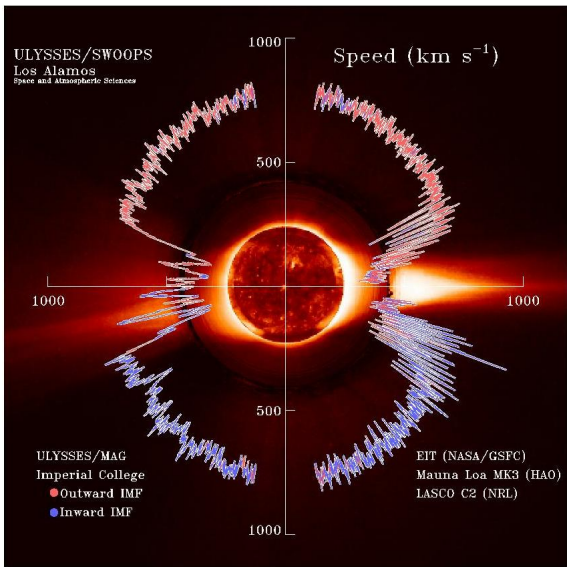

Figure 2.1: One-hour averages of the solar wind speed vs. the latitude of the Sun measured by Ulysses (NASA)

The current sheet is tilted because the Sun's rotation axis and magnetic dipole axis are different from each other (Ω and M in figure 2.2). The shape of the HCS can be compared to a ballerina skirt or a sombrero. The twisting of the HCS is due to the Sun rotating while solar wind is flowing out radially and waviness of the sheet is caused by the varying shape of the solar magnetic field.

As the Earth orbits around the Sun, it will cross the HCS in different "towards" and "away" sectors, this is solar Sector Boundary Crossings (SBC). When Earth crosses the HCS, the terrestrial magnetic field interacts with the IMF. The polarity of the B_x component defines the solar sector which is whether the IMF is flowing "towards" or "away" from the Sun. The solar sector determines if the reconnection of the magnetic field lines will occur in the northern or southern hemisphere.

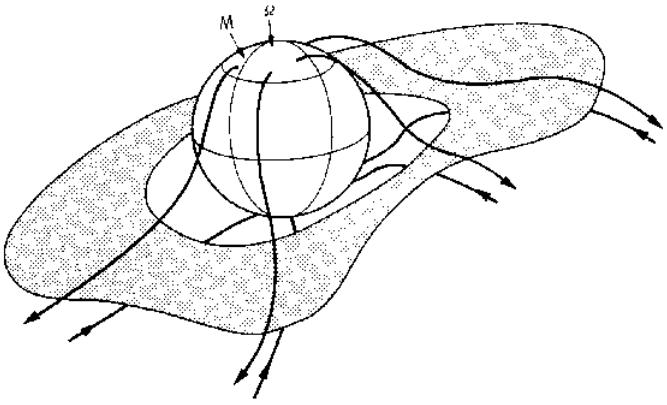

Figure 2.2: The shaded current sheet separates fields from the north and south solar magnetic poles which are open (only one end attached to the Sun). The normal to the current sheet (M) represents the magnetic axis of the solar field and is shown tilted with respect to the Sun's rotation axis (Ω). Closed field lines (those which have both ends on the Sun) are shown at mid-latitudes to low latitudes and lie inside the current sheet. The fields above and below the current sheet develop the spiral structure characteristic of the solar wind generally [Smith, 2001].

2.1.2 Coronal Mass Ejections

Coronal Mass Ejections (CMEs) are bubbles of plasma within the solar wind, bursting out of the solar corona and expanding the further out they get. CMEs are caused by solar magnetic field lines, that have been closed for several days or even weeks, getting opened. When the field lines are opened, they add material from the corona and the chromosphere to the flow that is ejected violently outwards. These CMEs can have velocities up to 2000 km/s [Lepping et al., 2001].

A CME can occur in the near-coronal environment or in the case of more powerful ejections they will travel further out and as interplanetary CMEs (ICMEs) [Lepping et al., 2003]. ICMEs reaching Earth are accompanied by shock waves of flowing solar plasma which, in interaction with Earth's magnetic field, will cause geomagnetic storms that can, in some strong cases of severe space weather, have consequences as power outages and disruptions in the GPS positioning data [Balan et al., 2014].

2.2 Plasma Physics

A plasma is defined as a quasi neutral gas of charged and neutral particles that exhibits collective behaviour [Chen, 1984].
In our universe matter can exist under four different states: solid, liquid, gaseous and plasma, the latter of which is ionized gas formed when a gas reaches very high temperatures or is exposed to radiation. Plasma does not exist naturally on Earth, however 99% of all visible matter in the universe are plasmas. In the heliosphere we are concerned with space plasmas. A space plasma, as all other plasmas, is composed of ionized particles that have no net charge when being averaged together, this corresponds to quasi neutrality. The ion and electron gases interact with each other and the plasma will move as one gas. Space plasmas manifest themselves in the Sun and stars by thermonuclear fusion, in the interplanetary, interstellar and intergalactic mediums. Plasmas can also be found as terrestrial plasma which concerns the near-Earth environment and atmosphere (lightnings, the ionosphere, auroras).

2.2.1 Single Particle Motion

Single particle motions describe how individual particles behave in electric and magnetic fields. It is assumed that there are no collisions or interactions between the particles and gives an overview of their expected trajectories.

The Lorentz force $\mathbf{F}$ defines how the electric and magnetic forces act on a particle when introduced to electromagnetic fields.

$$\mathbf{F} = q(\mathbf{E} + \mathbf{U} \times \mathbf{B}), \tag{2.3}$$

where, q is the charge of the particle, $\mathbf{U}$ the particle velocity, $\mathbf{E}$ and $\mathbf{B}$ are the electric and magnetic fields, respectively.

The particle's motion is described by inserting the Lorentz force into Newton's second law:

$$m(\frac{d\mathbf{U}}{dt}) = q(\mathbf{E} + \mathbf{U} \times \mathbf{B}), \tag{2.4}$$

where, m is the mass of the particle.

By assuming no electric fields and homogeneous magnetic fields and then resolving equation 2.4, the particle will rotate with the same orbit around a magnetic field line with a gyrofrequency Ω_c and Lamour radius r_c.

$$\Omega_c = \frac{qB}{m} \tag{2.5}$$

$$r_c = \frac{mU_\perp}{qB} \tag{2.6}$$

Introducing an electrical field $\mathbf{E}$ perpendicular to the magnetic field, the particle will continue to gyrate, but the electrical field will accelerate and decelerate (and thereby the Lamour radius will grow and shrink respectively) it, creating a drift. The particle's trajectory is now a cycloid. This constant motion perpendicular to both electrical and magnetic fields is called $\mathbf{E} \times \mathbf{B}$-drift ($\mathbf{U}_c$) and can be derived over one gyration (one period):

$$\mathbf{U}_c = \frac{\mathbf{E} \times \mathbf{B}}{B^2} \tag{2.7}$$

Any force capable of accelerating or decelerating a particle as it gyrates around $\mathbf{B}$ will create drifts normal to the magnetic field.

$$\mathbf{U}_f = \frac{\mathbf{F}_c \times \mathbf{B}}{qB^2}, \tag{2.8}$$

where, $\mathbf{U}_f$ is the drift caused by the introduced force field and $\mathbf{F}_c$ represents an arbitrary constant force. If this force is independent of the charge q, the electrons and ions would drift in opposite directions and give rise to currents.

2.2.2 Magnetohydrodynamics

Magnetohydrodynamics (MHD) is a model for the dynamics of fully ionized plasmas, as they are found in the upper atmosphere of the Earth, in the magnetosphere, or in more distant regions of space [Pécseli, 2013]. The model describes the plasma as one medium (a fluid) characterized by it's high conductivity and ignores the fact that a plasma is composed by a mixture of two "gases", an electron "gas" and one ion "gas" [Pécseli, 2013].

When there is no creation or loss of particles, the medium will follow the continuity equation:

$$\frac{\partial \rho}{\partial t} + \nabla \cdot (\mathbf{u}\rho) = 0, \tag{2.9}$$

where, ρ represents the mass density and $\mathbf{u}$ the velocity.

The Navier-Stokes equation describes the balance between the momentum density and the MHD-forces acting on the plasma.

$$\rho(\frac{\partial}{\partial t}\mathbf{u} + \mathbf{u} \cdot \nabla \mathbf{u}) = -\nabla p + \mathbf{J} \times \mathbf{B} + \rho \mathbf{g} \tag{2.10}$$

The forces acting on the fluid are the pressure gradient force ∇p, the $\mathbf{J} \times \mathbf{B}$ force due to currents flowing in the plasma giving rise to magnetic fields, and the gravitational force, $\rho \mathbf{g}$.

Faraday's law of induction relates the electrical and magnetic fields to each other:

$$\nabla \times \mathbf{E} = \frac{-\partial \mathbf{B}}{\partial t} \tag{2.11}$$

Ampère's law connects the rotation of the magnetic field $\mathbf{B}$ to the current density $\mathbf{J}$:

$$\nabla \times \mathbf{B} = \mu_0 \mathbf{J} + \frac{1}{c^2}\frac{\partial \mathbf{E}}{\partial t}, \tag{2.12}$$

where, μ_0 is the vacuum permeability and $\mathbf{E}$ is the electrical fied. The last term will be ignored for the case of plasma its variations are slow compared to the speed of light c.

Ohm's law is given by:

$$\mathbf{J} = \sigma(\mathbf{E} + \mathbf{u} \times \mathbf{B}) \tag{2.13}$$

with σ being the conductivity.

Divergence less $\mathbf{B}$ means that the magnetic flux over a closed surface is conserved:

$$\nabla \cdot \mathbf{B} = 0 \tag{2.14}$$

2.2.3 Frozen-in condition

For a highly conductive plasma, the concept of "frozen-in-field" implies that the the magnetic field lines are locked into the plasma and carried with it as it moves maintaining a constant magnetic flux [Alfvén, 1942].

In the previous section, Ohm's law was defined in equation 2.13. By rewriting this expression into

$$\mathbf{E} + \mathbf{u} \times \mathbf{B} = \frac{\mathbf{J}}{\sigma} \tag{2.15}$$

and the limiting to case of ideal MHD (highly conductive plasma) with the conductivity $\sigma \to \infty$. This implies that an electric field is induced by the motion of plasma across magnetic field lines. By inserting equation 2.15 into 2.11 and simplifying with equation 2.12, we obtain:

$$\frac{\partial \mathbf{B}}{\partial t} = \nabla \times (\mathbf{u} \times \mathbf{B}) + \frac{1}{\mu_0 \sigma} \nabla^2 \mathbf{B} \tag{2.16}$$

The first term on the right hand side of equation 2.16 corresponds to the magnetic field lines moving with the plasma (convective term) whilst the second term corresponds to the field lines moving through the plasma (diffusion term). By examining the ratio between the two terms and consider equation 2.16 dimensionally (letting $\nabla \to \frac{1}{l_0}$ and $\nabla^2 \to \frac{1}{l_0^2}$, where l_0 is the characteristic length scale of the system), the magnetic Reynold number R_m can be derived:

$$R_m = l_0 u \mu_0 \sigma \tag{2.17}$$

In cases of high conductivity or large scale sizes (such as in the solar wind, $R_m \sim 10^{11}$), the convection term is dominant and the frozen-in condition is valid ($R_m \gg 1$). In the Earth's magnetosphere, there are regions where the frozen-in condition breaks down (such as at the magnetopause) and the diffusion term will dominate, allowing magnetic reconnection between two different plasma regimes to occur.

2.3 IMF-Magnetosphere coupling

As the solar wind interacts with the Earth and deforms its magnetic field, a protective cavity called the magnetosphere forms around the planet. The magnetopause is the

boundary of the magnetosphere and separates the geomagnetic field with plasma of primarily terrestrial origin from the solar wind plasma (magnetosheath) [Kivelson and Russel, 1995]. The magnetosheath plasma has a weaker and also oppositely directed magnetic field than the magnetosphere which will give rise to a large scale current sheet named the magnetopause current or Chapman-Ferraro current. The nose of the magnetopause at the sub-solar point is located at the equilibrium between the solar wind dynamic pressure and the pressure in the magnetosphere (magnetic pressure).

$$\rho_{SW} u_{SW}^2 = \frac{B_{MS}^2}{2\mu_0}, \tag{2.18}$$

where ρ_{SW} is the density of the solar wind, u_{SW} is the solar wind speed, B_{MS} is the magnitude of the magnetic field at the magnetopause and μ_0 is the magnetic permeability in vacuum. The typical stand-off distance of the magnetopause is 10 R_e upstream of the Earth.

2.3.1 Magnetic Reconncection

Magnetic reconnection is the combination of two magnetic field lines permitting mixing of plasma from different origins. During the reconnection process, energy and mass are conserved as described by the continuity equation (equation 2.9). Magnetosheath plasma with the embedded IMF flows towards the geomagnetic field lines (marked by small orange arrows in figure 2.3) and will be compressed out on the sides as jets (after merging), as shown by big orange arrows in figure 2.3.

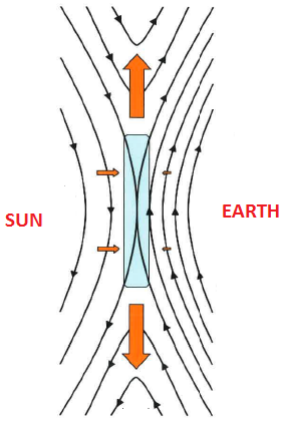

Figure 2.3: Illustration of an x-line assymetric reconnection based on the Cassak-Shay model [Cassak and Shay, 2007], adapted from Ouellette et al.(2010). The diffusion region is highlighted in blue.

The antiparallel field lines, originating from different regions, frozen into the plasma, give rise to thin current sheets as they approach. As the field lines become very close, the plasma particles get demagnetized (loose the ability to gyrate) and will move randomly which gives us the diffusion region, highlighted in blue in figure 2.3.

For an IMF $B_z < 0$ merging with a geomagnetic field in the opposite direction, the IMF will reconnect at the magnetopause.

2.3.2 Dungey Cycle

The Earth generates a magnetic dipole field originating from internal processes as the rotation of the Earth itself is associated with the creation of the magnetic field [Brekke, 2013]. The dipole field is tilted with an angle of 11.5°with respect to the rotational axis of the Earth and will change when it interacts with the solar wind and IMF. The field lines on the dayside of the Earth will be compressed by the solar wind, and then, through magnetic reconnection to the IMF, dragged towards the nightside and stretched outwards into an elongated tail.

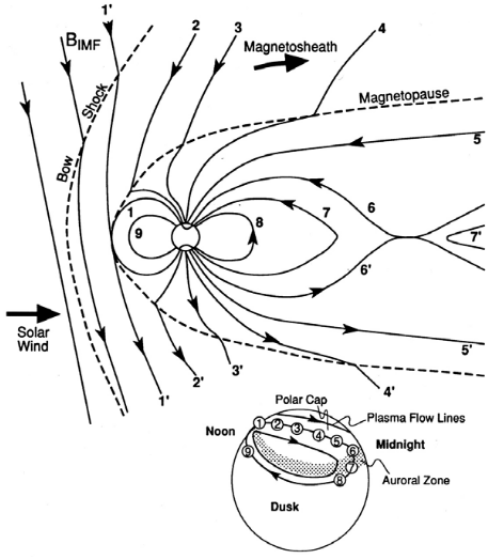

Figure 2.4: Cross section of the Dungey cycle in the noon midnight meridian. The smaller drawing shows the motion of the footpoint of the magnetic field lines in the ionosphere through the Dungey cycle.[Kivelson and Russel, 1995]

When the IMF is pointing southwards (B_z <0), it will reconnect with a closed terrestrial magnetic field line. The terrestrial field lines are then drawn back over the polar cap as the IMF is carried tailward by the solar wind. As the field lines are

stretched into a tail from both hemispheres, the oppositely directed field lines will generate a current system as they approach each other. This current system is called the cross tail current. The open field lines will reconnect on the nightside accelerating the plasma towards Earth [Dungey, 1961]. The motion of the magnetic field lines are shown in figure 2.4.

- (1) Reconnection of the IMF (1') with the geomagnetic field (1) at the magnetopause.
- (2) – (4) The open field lines are dragged back over the polar cap and stretched as the IMF is carried tailward by the solar wind.
- (5) The stretched open field lines sink into the tail region of the magnetosphere.
- (6) The oppositely directed open field lines reconnect on the nightside. Plasma is accelerated along the magnetic field lines towards the Earth.
- (7) Dipolarization of the newly closed terrestrial magnetic field lines.
- (8) - (9) The closed field lines are convected back to the dayside magnetosphere.

Stages (1) to (4) described above also give rise to the main topic of this thesis: the dayside aurora. After reconnection in the magnetopause, solar wind plasma is accelerated directly into the upper atmosphere, interacting with its constituents and thereby creating auroral emissions.

2.3.3 Regions of the Magnetosphere

The interaction between solar wind and the magnetosphere give rise to different boundary regions and current sheets within the magnetosphere, illustrated in Figure 2.5. Spacecraft crossings through the magnetosphere have identified five different regions: LLBL, Cusp, Mantle, CPS and BPS based on plasma particle characteristics as density, energy, velocity and the magnetic environment in which they occur.

The Low-Latitude Boundary Layer (LLBL) extends across the dayside and nightside region with newly opened field lines permitting the the entry of magnetosheath plasma that will mix with the magnetospheric plasma. This mixture of plasma particles drifting in different directions give rise to the magnetopause current. As the LLBL extends over the whole nightside, it acts as a border between the plasma sheet and the magnetosheath. The cusp is situated on high latitudes ranging over three hours on both sides of magnetic noon. It serves as an entry boundary layer and will therefore

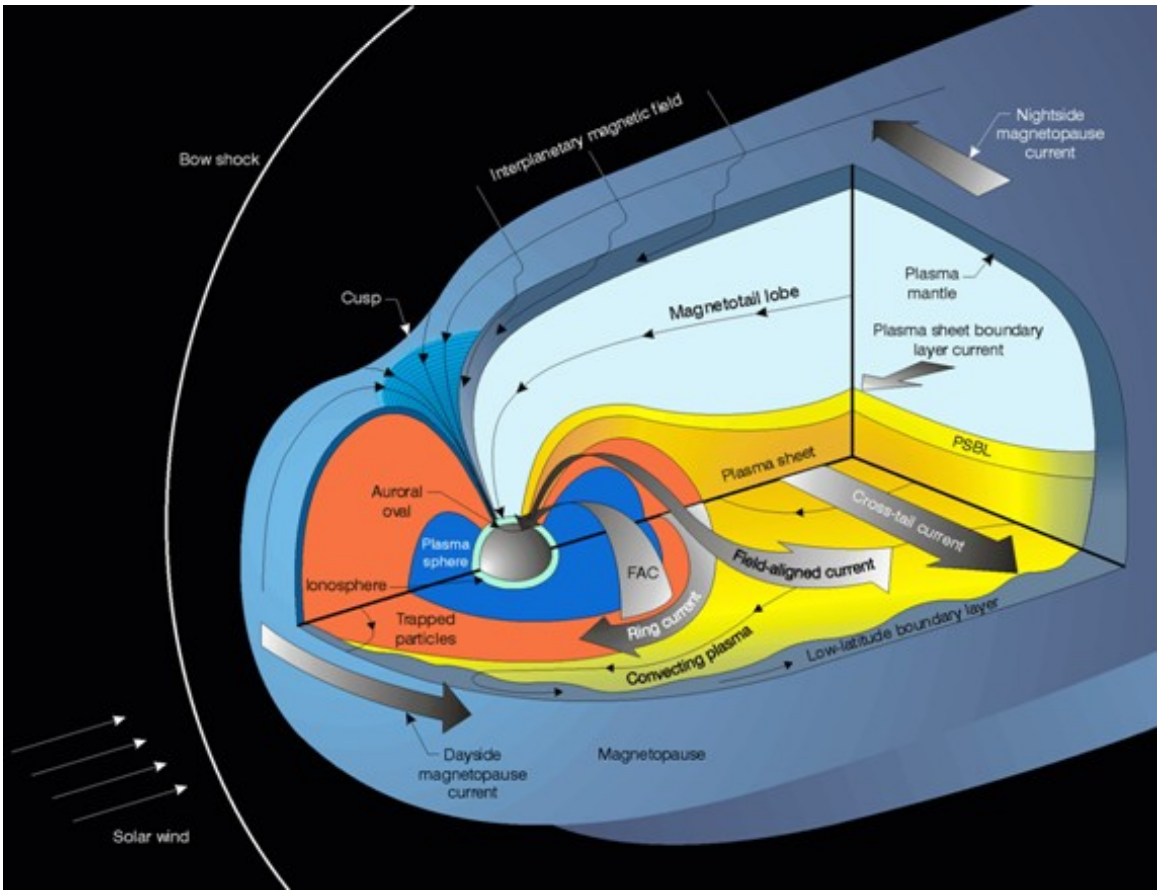

Figure 2.5: Schematic of the magnetospheric boundary regions and current systems. Adapted from [Russell et al., 1995]

essentially contain plasma of magnetosheath origin. The plasma mantle is located on high latitudes tailward of the cusp. In this region, the plasma flow (originating from both the magnetosheath and the magnetosphere) is always towards the tail on both open and closed field lines separating the tail lobes from the magnetosheath. On the nightside, the Boundary Plasma Sheet (BPS) is separating the Central Plasma Sheet (CPS) from the tail lobes. It contains magnetospheric plasma accelerated towards both the tail and Earth from the reconnection point in the tail forming a current sheet called the Plasma Sheet Boundary layer current. As these accelerated particles reach the near-Earth region, they will get trapped on closed field lines and bounce back and forth on the mirror points, creating the ring current, before they return to the CPS giving rise to the field aligned currents closing in the cross tail current. This latter current is formed by the oppositely directed field lines approaching each other before the reconnection in the tail [Kivelson and Russel, 1995]. The field aligned currents will be discussed in more detail in section 2.4.2.

In order to study the dayside aurora, it is important to have an understanding of where in the magnetosphere the particles originate from. In this analysis, all auroral structures observed from 0600 - 1800 MLT is considered dayside aurora. Newell and Meng, 1992, studied 60 000 individual low-latitude satellite passes through the daytime auroral oval in order to determine different boundary regions based on plasma characteristics mapped down to the ionosphere. These regions have briefly been discussed in section 2.3.3. The statistically identified regions are presented in a MLAT/MLT (Magnetic Latitude/Magnetic Local Time) coordinate system in Figure 2.6.

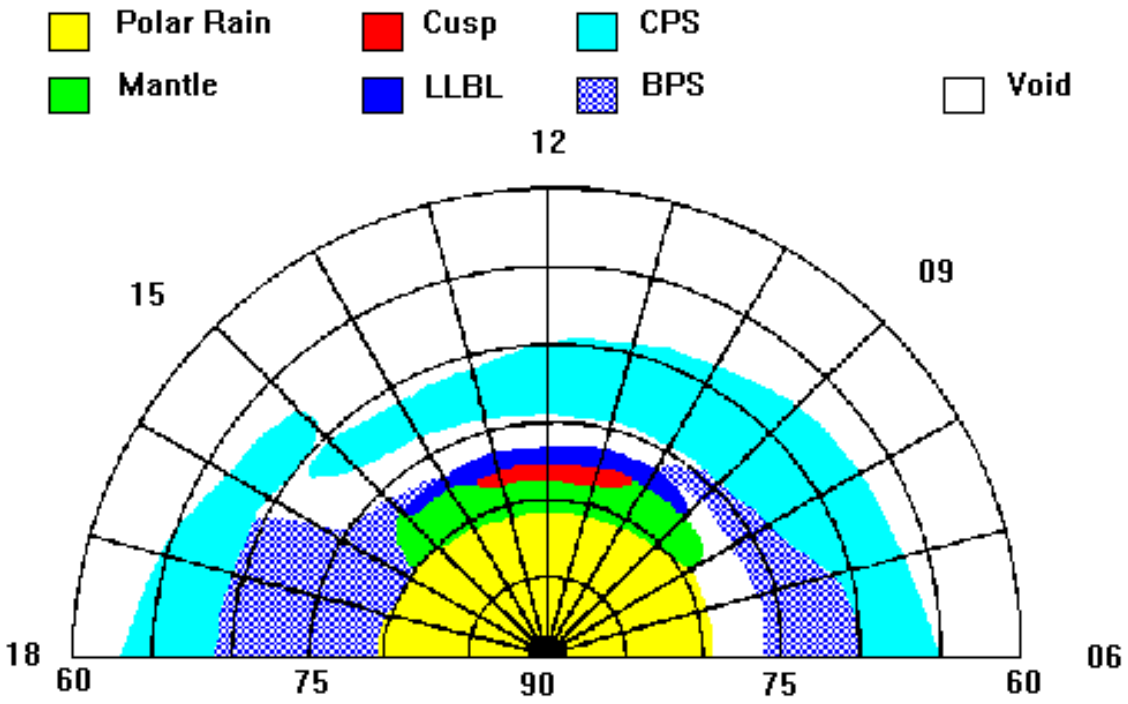

Figure 2.6: Statistical mapping of the dayside ionosphere to the magnetosphere for all IMF and magnetic activity conditions [Newell and Meng, 1992].

The cusp is confined to a narrow area at 78°with a thickness of 0,5 to 1 MLAT over "cusp times" at 10.00 to 14.00 MLT. It is recognised by its open field lines permitting direct entry of magnetosheath plasma [Newell and Meng, 1992]. The particles in the cusp have a very high flux and low energies (<1 keV for electrons and 1-4 keV for protons). The Low Latitude Boundary Layer (LLBL) has both closed and newly opened field lines allowing mixture of magnetosheath and magnetospheric plasma. The particle flux is around ten times lower than in the cusp, but the particles are slightly more energetic in the LLBL. The Mantle is composed of de-energized

magnetosheath plasma with both particle flux and particle energies at lower levels than in the cusp [Newell et al., 1991]. The Central Plasma Sheet (CPS) and Boundary Plasma Sheet (BPS) are precipitation regions from the nightside extended into the dayside. They exist on closed field lines with a low flux of medium to high particle energies (>20 keV for both ions and electrons in the CPS and 1-10 keV for electrons and 4-10 keV for ions in the BPS).

2.3.4 Ionospheric Convection and it's relationship to IMF B_z and B_y

The Dungey cycle described in section 2.3.2 sets up a flow of ambient plasma in the F-region of the ionosphere, controlled by the motion of the IMF and terrestrial magnetic field. The IMF carries an electric field system that is mapped down to the ionosphere and give rise to a horizontal $\mathbf{E}\times\mathbf{B}$-drift (equation 2.7) termed ionospheric convection. This flow is shown for a variety of IMF B_z and B_y configurations in figure 2.7. In the case of IMF southwards (B_z <0), the plasma convection (solid lines) consists of twin vortexes, with antisunward flow over the polar cap which maps to the magnetospheric tail lobes, and return sunward flow in the auroral region, which maps mainly to the central plasma sheet and ring current regions (cf. chapter 2.3.3 [Cowley, 2000]).

In the case where B_y ∼0 (middle panels, figure 2.7), the convection pattern is symmetric around the noon-midnight meridian. The open closed field line boundary (OCB) located in the cusp region marks the ionospheric footprint of the reconnection point. The introduction of a B_y component will add an asymmetry to the system which will be discussed below. The contribution of the the B_y component will tilt the direction of the IMF and shift the mapping of dayside reconnection point to the ionosphere towards dawn or dusk. For B_y <0, the IMF is directed southeastward and the reconnection footprint is moved to earlier MLTs, the dawn sector. The dusk convection cell expands to earlier MLTs while the dawn lobe cell expands over the polar cap. For the B_y >0, the situation is reversed. The southwest directed IMF will map the reconnection point to later MLTs, the dusk sector and the dawn cell expands to later MLTs. The dusk lobe cell expands across the polar cap [Brekke, 2013]. These cases are illustrated in the top left and right panels of Figure 2.7.

When the IMF is directed northward (B_z >0), reconnection will occur in the tail lobes, creating a more complex convection geometry. For the simple case of B_y=0, two lobe cells are located within the polar cap surrounded by one expanded viscous cell on

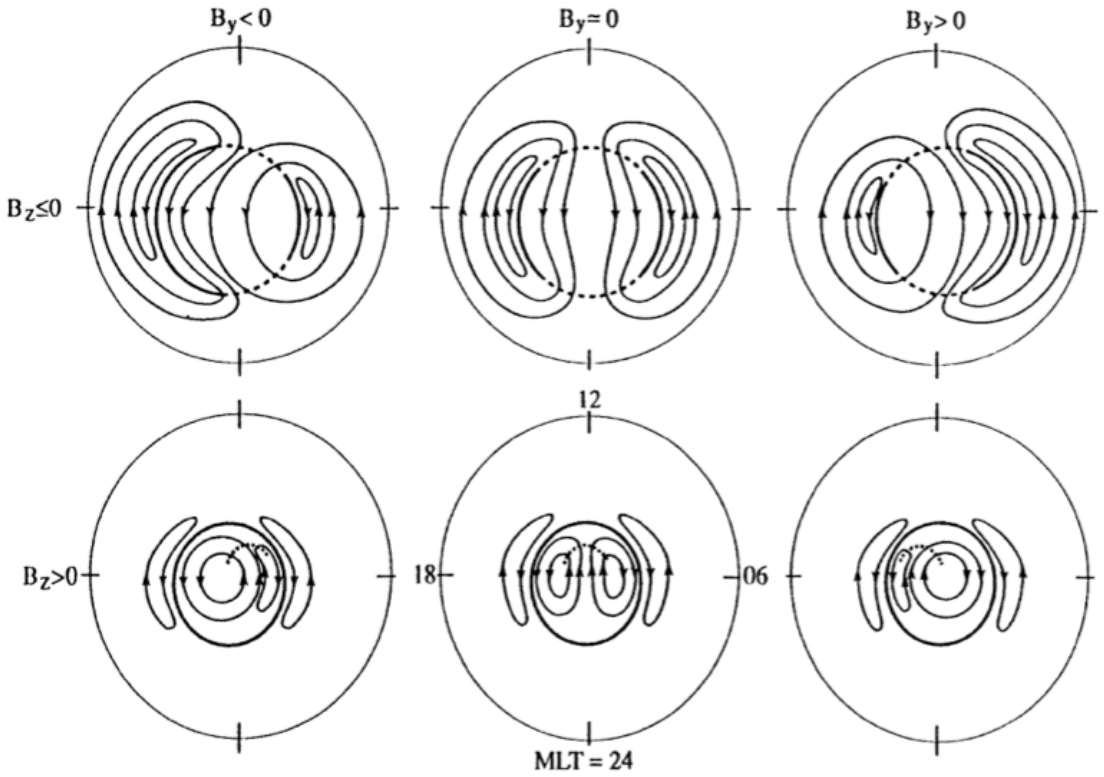

Figure 2.7: Dungey-cycle flow mapped into the ionosphere as a high latitude convection pattern in the magnetic latitude-magnetic local time coordinate system for different orientations of the IMF. The lines with arrows represent the plasma convection. The centered circles represent the OCB (Open-closed field line Boundary). The dashed lines in the upper panels, for southward IMF, are the footprints of the reconnection sites in the magnetopause. The dashed lines in the lower panels, northward IMF, are the footprints of the reconnection sites in the tail lobes [Cowley, 1998].

lower latitudes in both the dawn and dusk sector, as shown in the middle bottom panel of figure 2.7. With contribution from the B_y component, the weaker northward oriented IMF induces a three celled convection pattern with oppositely directed flows for B_y <0 and B_y >0 [Brekke, 2013], which can be observed in the bottom left and right panels of figure 2.7. It can thus be seen that since the orientation of the IMF effects, amongst other things, the ionospheric flow direction and the location of the OCB it will also effect the topology of the auroral signatures observed at particular MLTs.

2.4 The Ionosphere

2.4.1 Composition

The Earth's atmosphere is divided into layers based on the relationship between altitude and temperature. Closest to the surface is the troposphere, then follows the stratosphere, mesosphere, thermosphere and exosphere at 800 km altitude. Due to ultraviolet radiation from the Sun, the upper level of the atmosphere (higher part of the mesosphere, the thermosphere and the lower part of the exosphere) from 60 to 1000 km altitude is partly ionized. This region is called the ionosphere.

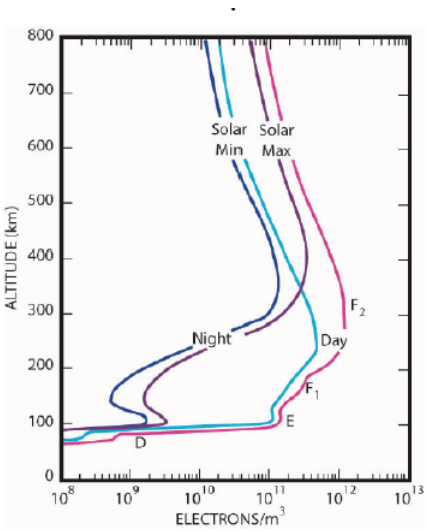

Figure 2.8: The ionosphere divided into layers based on plasma density as a function of altitude.

The ionosphere is divided into 3 main layers: a D-region from 60 to 90 km above the terrestrial surface, an E-region between 90 and 130 km and a F-region above 130 km altitude. An altitude profile of ionospheric density is seen in figure 2.8 with the different regions marked. The lower part of the ionosphere, the D-region, is a daytime phenomenon. It is weakly ionized due to the high occurrence of atmospheric particles. The upper ionosphere consists of the E- and F-regions and is partially ionized. These two regions have different particle densities during the day and the night and their boundary is more distinguishable during the night. The E-region is created primarily through two main mechanisms: through the absorption of UV radiation on the dayside and by ionization from energetic particle populations on the nightside. At higher altitudes, the F-region can be separated into two regions: F_1 at 200 km altitude and F_2 at 300 km. F_1 is mainly a dayside phenomenon formed by absorption of UV

radiation of shorter wavelength by different molecules. The F_2-region, on the other hand, is present both on the day- and nightside. It's formation is due to collisional ionization by incoming particle populations from the magnetosphere/solar wind. The peak in the plasma density occurs at around 300 km altitude, the so-called F_2 peak [Baumjohann and Treumann, 1996].

On the dayside, the particle flux is high ($10^{14} m^{-2} s^{-1}$) and particle energies are low (0.1 keV) meaning that the maximum production rate (maximum ionization due to electron precipitation) will be located at higher altitudes, around 200 km, in the F-region. On the nightside, the particle flux is lower than on the dayside ($2 \times 10^{13} m^{-2} s^{-1}$) and particle energies are high (5 keV) which will enable the particles to penetrate deeper in the ionosphere as the maximum production rate is situated at around 110 km altitude, in the E-region [Sandholt et al., 2002, Strickland et al., 1983].

2.4.2 Current systems in the ionosphere

As already mentioned in the discussion of the Dungey cycle in chapter 2.3.2, after reconnection at the magnetopause, the field lines will move across the polar cap over to the nightside. The footprint of the field lines in the ionosphere will map out the plasma convection pattern discussed in chapter 2.3.4. This flow is driven by the solar wind dynamo in where the solar wind electric field is mapped down the magnetic field lines, creating the large scale dawn-dusk convection electric field. Ionospheric currents flow both parallel and perpendicular to the magnetic field. Two types of currents perpendicular to the magnetic field arise: Pedersen currents flowing parallel to the electric field and Hall currents perpendicular to the electric field [Kivelson and Russel, 1995]. Field aligned currents (FAC), also called Birkeland currents, flow parallel to the magnetic field and are responsible for the transfer of energy between the magnetosheath and the magnetosphere [Cowley, 2000]. Since they are field aligned, the Birkeland currents flow in both E-and F-regions. The ionospheric current system $\mathbf{j}$ can be described by Ampéres law (equation 2.12) considering contributions from Pedersen, Hall and Birkeland currents:

$$\mathbf{j} = \sigma_P \mathbf{E}_\perp - \sigma_H \frac{\mathbf{E} \times \mathbf{B}}{B^2} + \sigma_\parallel \mathbf{E}_\parallel \tag{2.19}$$

where σ_P, σ_H and $\sigma_\parallel$ represent the Pedersen, Hall and Birkeland conductivities respectively. $\mathbf{E}_\perp$ and $\mathbf{E}_\parallel$ are the perpendicular and parallel components of the electric

field **E** with respect to the magnetic field, **B**.

The large scale Hall and Pedersen currents are shown in figure 2.9. The Hall currents are indicated by the yellow lines and flow anti-parallel to the convection flow. The Pedersen currents are indicated by the orange lines and flow across the auroral oval, allowing current closure of the FAC in the ionosphere. Also shown is the smaller magnitude Pedersen currents associated with the aforementioned large scale cross polar cap electric field, flowing from dawn to dusk.

There are two types of field aligned currents: Region 1 currents (R1) are higher latitude currents flowing into the ionosphere at dawn and out at dusk, and Region 2 currents (R2) flowing at lower latitudes entering the ionosphere at dusk and exiting at dawn. The Region 1 system flowing in the vicinity of the open-closed boundary is fed by the Pedersen current flowing from dawn to dusk across the polar cap as well as by Pedersen currents streaming across the auroral region [Cowley, 2000], as shown in figure 2.9.

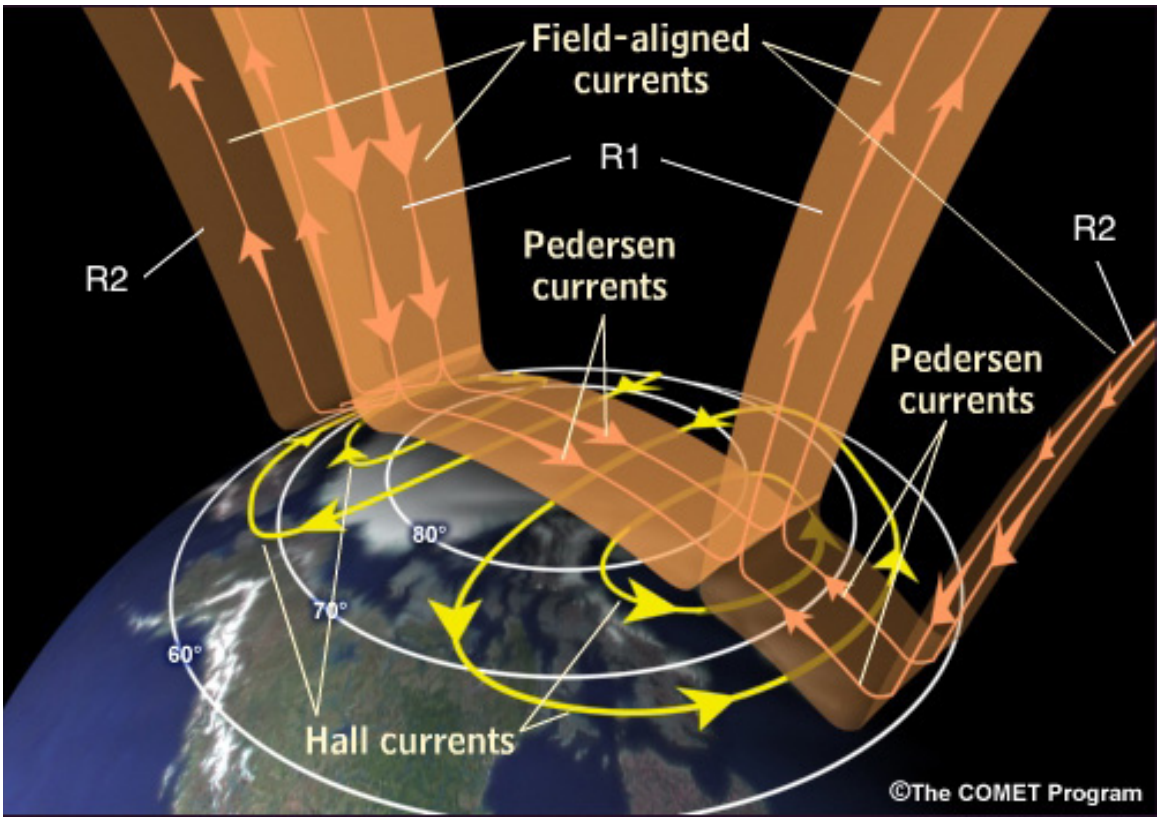

Figure 2.9: Ionospheric current systems seen from above the magnetic north pole. (Illustration adapted from The Comet Program, UCAR)

The FACs also provide a conduit through which magnetospheric current systems are

connected to the ionospheric Pedersen current systems. Figure 2.10 illustrates this large scale circuit system as viewed from the magnetotail. The magnetoapause current system is connected to the ionosphere through region 1 currents, whilst the partial ring current (which flows in the inner plasma sheet region) is connected through region 2 currents. The large scale Pedersen currents which flows across the auroral oval, then complete the circuit. A third type of FAC exist on open field lines on the dayside, poleward of the R1 currents, named R0 cusp currents. This current sheet is induced by the oppositely directed magnetosheath and magnetospheric plasma flowing towards each other in the cusp region [Cowley, 2000].

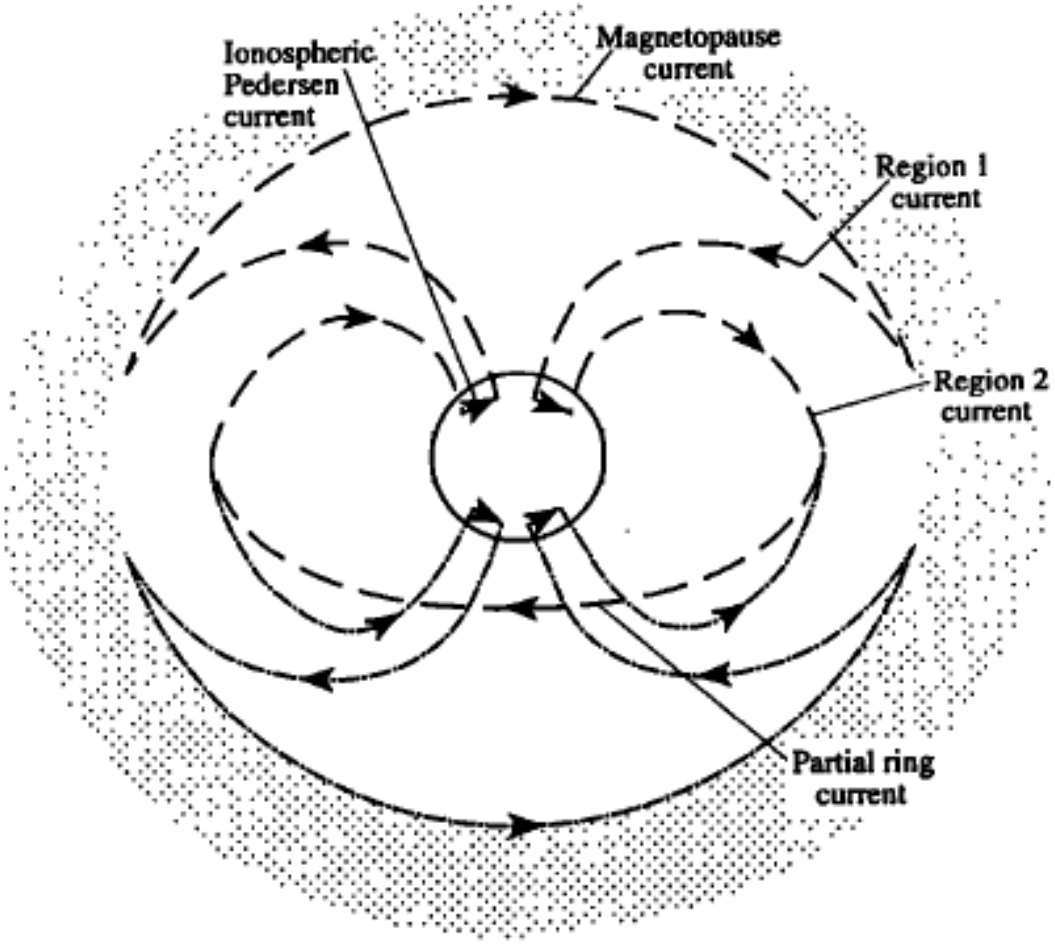

Figure 2.10: Overall auroral region current circuit seen from the tail. From Cowley, 2000 [Cowley, 2000].

Chapter 3

Auroral Physics

The dayside and nightside aurora have different properties due to the fact that they receive electron precipitation from different mechanisms. The nightside aurora is created from particles injected into the upper atmosphere after reconnection on the nightside (in the tail) and gyrate along the field lines and into the polar regions. The projection of auroral particles into the atmosphere form the auroral oval typically expanded to lower latitudes down to 67°MLAT on the nightside and 77°MLAT on the dayside. The day sector is defined to the time span between 06.00 and 18.00 MLT corresponding to the Earths orientation towards the Sun. All auroral structures observed within this time range are considered dayside aurora. The dayside high latitude aurora consists of forms with different plasma sources, which can be either of solar wind origin or of inner magnetosphere origin [Sandholt et al., 1998]. The different auroral forms and activities observed on the dayside are strongly related to the reconnection geometry, regulated by the IMF-orientation, and the resulted energy and momentum transfer between the solar wind and the magnetosphere-ionosphere coupling [Sandholt et al., 2002].

3.1 Spectrum

Different auroral emissions each correspond to a certain atmospheric constituent colliding with charged particles injected into the ionosphere from the solar wind, resulting in an auroral spectrum ranging from ultraviolet to infrared wavelengths. In the case of the auroral oval, this injection takes place when open magnetic field lines are closed in the magnetotail before being convected round to the dayside (stages 6 - 9 in the Dungey Cycle in figure 2.4). In the case of the dayside cusp, this injection of particles

happens on newly opened field lines (stage 1 in the Dungey cycle in figure 2.4). Auroral particles includes both electrons and ions with energies ranging from less than 100 eV to a few 100 keV. During the interaction between the incoming charged particles and the atmospheric particles, kinetic energy is converted into chemical energy and stored in the excited states of the atmospheric species. They will emit photons of different wavelengths, thus different colours. The most common colours of aurora are blue, green and red. The red aurora (630.0 nm) originates from precipitating particles in the F-region colliding with atomic oxygen (OI). The transition of the oxygen atom above 200 km altitude is a forbidden transition (does not obey the rules of quantum mechanics meaning that the oxygen stays in an excited state for a longer amount of time before it relaxes to a lower energy state) and has therefore a long lifetime (110 s). The oxygen atom will then suffer a collision that will knock out its current energetic state before it has the chance to emit a photon, this is called collisional quenching. As demonstrated in figure 3.1, the red auroral emission line is due to the ^1D state relaxing to the ground state and will be visible at 150 to 300 km altitude. Figure 3.1 also shows 636.4 nm emissions when the ^1D state relaxes to ^3P state which is a fine structure of the electron shell in the ground state [Sandholt et al., 2002]. The green aurora (557.7 nm) is also a result of a forbidden transition of OI, but has a shorter lifetime of only 0.7 s. The transition is shown in figure 3.1 by an electron relaxing from the ^1S excited state to ^1D state. Green auroral emissions are typically observed between 100 to 130km altitude, much lower than red auroral emissions. Red aurora is typically associated with particle energies of around 0.1 keV whilst green aurora is associated with particles of energies ranging from 1 to 10 keV. The particles that are responsible for the red aurora are not energetic enough to penetrate deep into the ionosphere which results in the high altitude location of the red emission line. The blue aurora (427.8 nm) is a result of charged particles colliding with N_2 in the E-region. Hence, blue auroral emissions are observed at the lowest altitude.

3.2 Auroral Structures

The aurora has been classified in many ways depending on their origin and form. Electron auroras can be divided into discrete and diffuse auroras based on their intensity. Discrete auroras are the result of electrons accelerated along field lines down to the atmosphere where they collide with neutrals. They are observed as clear and intense

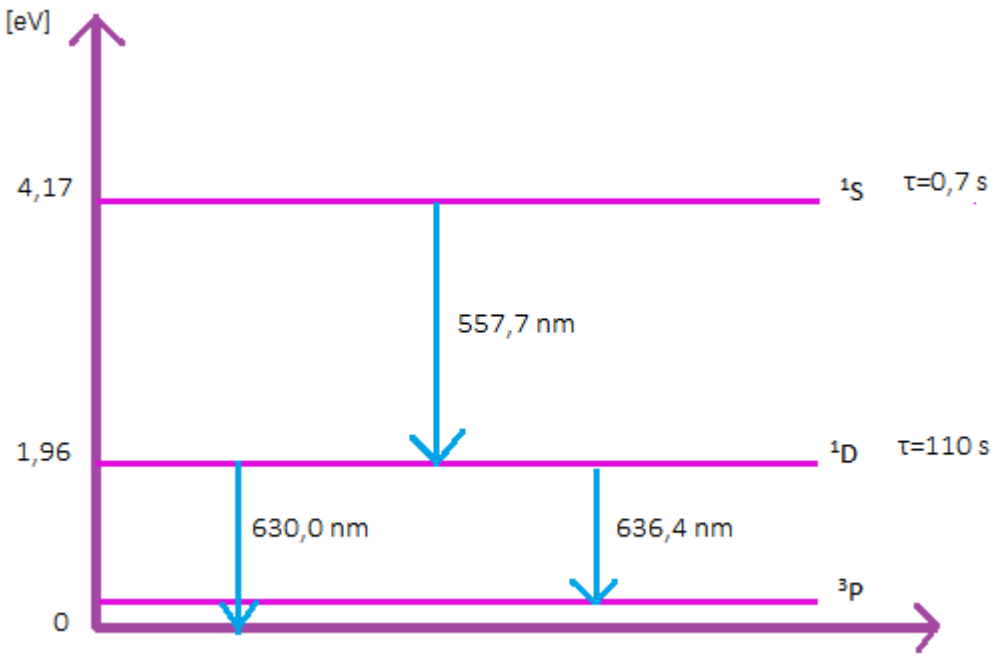

Figure 3.1: Energy level diagram of the oxygen atom with the half-lives τ of the ^1S (0.7 s) and ^1D (110 s) energy levels. Their emitted photons after relaxation are of wavelengths 557.7 nm (green emission line) and 630.0/636.4 nm (red doublet).

structures. The discrete aurora is typically shaped as a quiet homogeneous arc spanning from east to west in a straight or curved line following the natural shape of the auroral oval. With increased geomagnetic activity, the aurora gets more dynamic and the quiet arcs breaks up into shapes like folds, spirals and curls [Hallinan and Davis, 1970]. During an auroral substorm (auroral response to an ordered sequence of events that occurs in the magnetosphere and ionosphere when the IMF turns southward and an increased amount of energy flows from the solar wind into the ionosphere [McPherron, 1979, Akasofu, 1979, Rostocker et al., 1980]), quiet arcs forms into an auroral bulge moving poleward in the midnight sector. In the recovery phase of an auroral substorm, discrete aurora can be observed as large scale folds named omega bands from their shape as the Greek Ω character [Akasofu, 1974]. These discrete structures are mainly nightside auroral phenomena originating from the dynamics of the geomagnetic tail and are located poleward of the auroral oval. Some discrete forms may also be present on the dayside, essentially in the cusp region receiving direct input of magnetosheath plasma after reconnection in the magnetopause [Sandholt et al., 1998].

On closed field lines, inside the auroral oval, diffuse aurora is caused by highly en-

ergetic particles gyrating along field lines back and forth between the northern and southern hemispheres until they are absorbed by the atmosphere. More precisely, these particles are trapped between two mirror points (the point at which the velocity component of the particle parallel to the magnetic field is zero). As a particle moves between its two mirror points it undergoes collisions (both with other particles and waves) which acts to reduce it's pitch angle. At some point the particle becomes scattered into the ionospheric loss cone permitting further collisions with atmospheric components and resulting auroral emissions. Each particle may gain a pitch angle, which is the ratio between the parallel and perpendicular components of the particles velocity changes, by colliding with a plasma wave reducing its pitch angle and scattering it into a loss cone permitting further collisions with atmospheric components. The diffuse aurora is dim and weak (1-2 kR [Lui and Anger, 1973]) without clear structures, but may contain some weak discrete forms [Kivelson and Russel, 1995]. It is mainly observed equatorward of the auroral oval as a result of CPS precipitation from the inner plasma sheet on closed field lines [Lui and Anger, 1973]. Pulsating auroras (aurora with repetitive varying in the intensity of the luminosity) and black aurora (downward FAC resulting in electrons being accelerated upwards and giving no visible aurora) may be observed in the diffuse region. Diffuse aurora can also be observed at lower latitudes when particles from the ring current interact with atmospheric components.

3.3 Dayside Aurora

All auroral structures observed between 06.00 and 18.00 MLT will, in this study, be considered as dayside aurora. Building upon the work of Newell and Meng (1992) discussed in chapter 2.3.3, Sandholt et al. (2002) classified six dayside auroral displays by using observations from satellite crossings, all-sky camera images and meridian scanning photometer stack plots. The results are illustrated in figure 3.2.

The cusp region is located in the midday sector and presents a clear distinction in auroral forms and activity from those existing in the morning and postnoon sectors. The cusp aurora is a subset of the dayside aurora. It represents the footprints of the direct entry of magnetosheath plasma and is therefore highly susceptible to the dynamics in the solar wind-magnetosphere coupling and thus solar wind parameters like bulk velocity and IMF orientation. There are two characteristic cusp auroral forms depending on the orientation of the IMF B_z component. The type 1 aurora

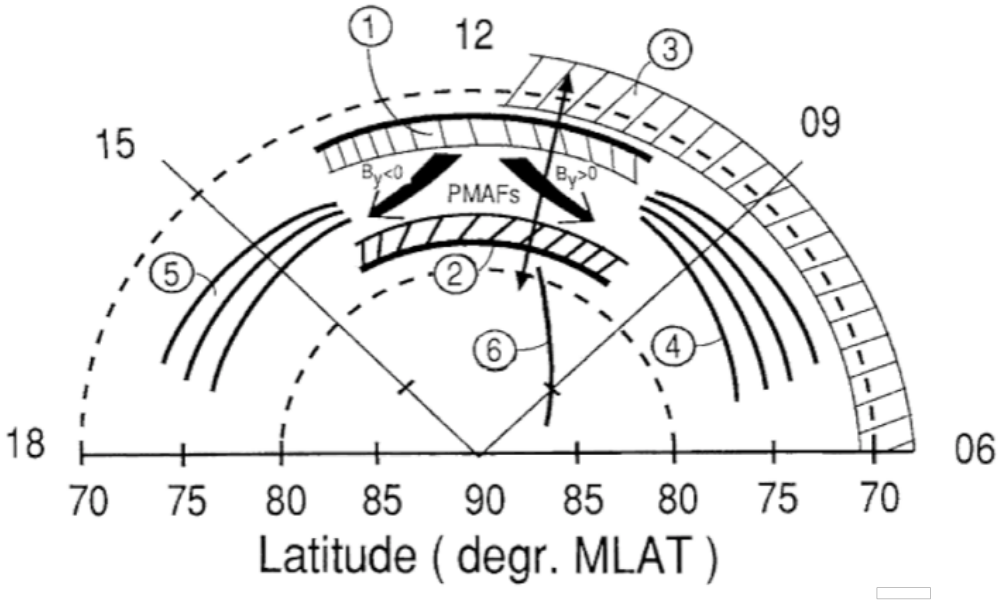

Figure 3.2: Schematic illustration of six dayside auroral forms for different orientations of the interplanetary magnetic field depending on its B_y component [Sandholt et al., 2002].

is due to the precipitation of magnetosheath plasma for a southward IMF B_z. It is typically present at 08.00 to 15.00 MLT and 70-75°MLAT [Sandholt et al., 2002]. The structure of the aurora is rayed bands with the red 630,0 nm emission line dominating and strong enhancements in the green line. Poleward Moving Auroral Forms (PMAFs) are mainly observed in the 630.0 nm emissions although some associated signatures are observed in the 557.7 nm emissions. These green emissions are also included in the type 1 aurora and their motion depends on the polarity of the IMF B_y component. This is shown by bold arrows in Figure 3.2. For B_y >0, the footprint of the cusp will move to into the postnoon sector with the type 1 aurora. PMAFs will move toward northwest with the background convection flow. For B_y <0, the footprint of the cusp with the type 1 aurora will expand into the prenoon sector and PMAF will move toward northeast. Type 2 aurora is also a cusp region phenomenon, but for northward oriented IMF B_z and is also due to accelerated magnetosheath plasma. It is located on higher latitudes, 75 to 80°MLAT, than the type 1 aurora. The form is an east-west emission bands (both 557.7 nm and 630.0 nm are present) with long rays [Sandholt et al., 2002]. These forms occur mainly in the pre-and postnoon sectors depending on the IMF B_y polarity. During steady IMF conditions, the type 2 aurora may be weak and calm with low intensities for the green emission line

making it difficult to detect, which is thereby named "midday gap aurora" [Dandekar and Pike, 1978]. Discrete auroral forms with higher green line intensities are observed at the equatorward and poleward boundaries of the cusp [Øieroset et al., 1997]. The mid-morning diffuse aurora is named type 3 aurora and is typically present from 08.00 to 11.00 MLT equatorward of prenoon discrete structures. This aurora type is mainly dominated by the green emission line and is due to precipitation of highly energetic magnetospheric electrons, originating from the plasma sheet, drifting around from the nightside [Sandholt et al., 2002]. As illustrated in figure 3.2, the type 3 aurora is observable for all configurations of the interplanetary magnetic field. Type 4 aurora correspond to mid-morning (08.00-10.00 MLT) multiple arcs. The particle precipitation in this region comes from mixed magnetosheath and magnetosphere plasma flowing sunward which is characteristic of the BPS [Sandholt et al., 1989]. The auroral arcs located further north within this sector are mainly dominated by the red emission line which corresponds to LLBL precipitation [Sandholt et al., 1989]. In the post-noon sector (13.00-16.00 MLT), recurring bright auroral arcs are observed and are called type 5 aurora. These arcs are also observed as spirals located within the sunward plasma convection, near the convection reversal boundary [Moen et al., 1994]. The particle precipitation is, as for the type 4 aurora, originating from the BPS which is the dayside extension of the plasma sheet [Sandholt et al., 2002]. By comparing figure 2.6 with figure 3.2, the mid-morning sector (09.00-10.00 MLT/74-78°MLAT) and the post-noon sector (14.00-16.00 MLT/74-78°MLAT), both the type 4 and type 5 auroras relate to the precipitation of BPS plasma. The type 6 aurora, in figure 3.2 is the designated polar-cap sun-aligned arcs occuring in the prenoon sector (08.00-12.00 MLT). These arcs are dominated by the 630,0 nm emission line and are moving antisunward across the polar cap from noon towards midnight [Sandholt et al., 2002]. As this study focuses on the 557.7 emission line, this auroral type will not be discussed further.

Chapter 4

Methods

The archipelago of Svalbard is located at 78 °N 16 °E. The tilting of the Earth's rotation axis with respect to the ecliptic plane causes the northern polar regions to lean away from the Sun during the winter season. These regions will therefore experience the polar night. During the polar night at Svalbard, the Sun stays below the horizon and the location right under the cusp makes it possible to observe and measure dayside aurora with optical instrumentation.

4.1 Instrumentation

4.1.1 All Sky Camera (ASC)

An All Sky Camera (ASC) is a camera with a high light sensitivity equipped with a fish eye lens connected to a camera with a CCD (Charged Coupled Device) detector. The lens has an observable view of 360°azimuth and 180°elevation.

The FMI (Finnish Meteorological Institute) All-Sky Camera has a filter wheel in order to observe the red, green and blue lines (λ=630.0 nm, λ=557.7 nm and λ=427.8 nm respectively) separately. The camera has a 20 seconds time resolution for λ=557.7 nm and 60 seconds time resolution for λ=427.8 nm and λ = 630.0 nm. It also has a pixel resolution of 512 $\times$ 512 corresponding to a mean spatial resolution of around 1 km the altitude of 110 km (ionospheric altitude). The camera is operable during the auroral season from October to end of February on Svalbard.

Figure 4.1 display the different components of the FMI All-sky camera [Syrjäsuo, 1996]. The entrance optics is a fish eye lens with an angular field of view of 180°permitting

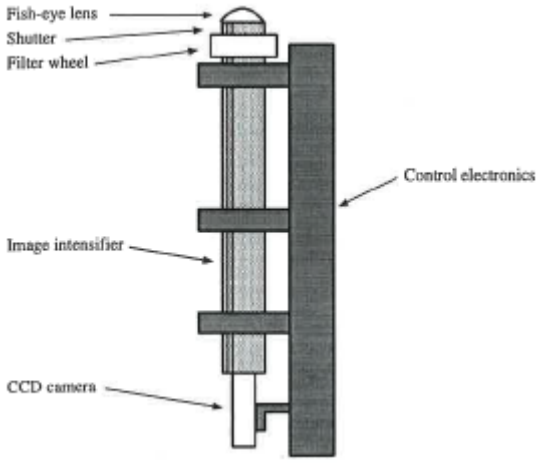

Figure 4.1: Components of the FMI All-sky camera [Syrjäsuo, 1996].

the whole sky to be imaged. Between the lens and the image intensifier, a shutter and a filter wheel are installed. The shutter protects the filter and image intensifier against exposure to direct sunlight. The filter wheel is composed of 3-inch filters of wavelengths 427.8 nm, 557.7 nm and 630.0 nm. The image intensifier permits the transformation of a low light level image into an amplified output image. The incoming photons are hitting a photocathode and due to the photoelectric effect, electrons will be emitted. These electrons will be accelerated and hit a microchannel plate that detects the electrons and multiplies them into secondary electrons. The electrons will then collide with a phosphor screen that will convert every electron into a photon. This results into an enhanced output image. A CCD camera is coupled to the output image from the image intensifier. The CCD detector contained in the camera is covered in silicon and the incoming photons hit the silicon layer within one pixel and are absorbed if they have the right wavelength [Howell, 2006]. Finally, the control electronics contains the all-sky camera electronics connected to a computer reading in the images.

MIRACLE (Magnetometer Ionospheric Radars All-sky cameras Large Experiment) is an instrument network, containing magnetometers, GPS receivers and all-sky cameras, spread across Fennoscandia and Svalbard in order to study the coupling between the magnetosphere and the ionosphere, run by the Finnish Meteorological Institute with international collaborators. The instruments are located within the auroral oval and polar cap to observe mesoscale auroral structures [FMI]. In this study, the All Sky Camera stations at Svalbard, Longyearbyen (LYR) and Ny-Ålesund (NAL), have been utilized to observe the auroral structures during cusp times. The daytime aurora

is only observable by the northernmost MIRACLE stations on Svalbard because of their location within the cusp region and the polar night from November to February.

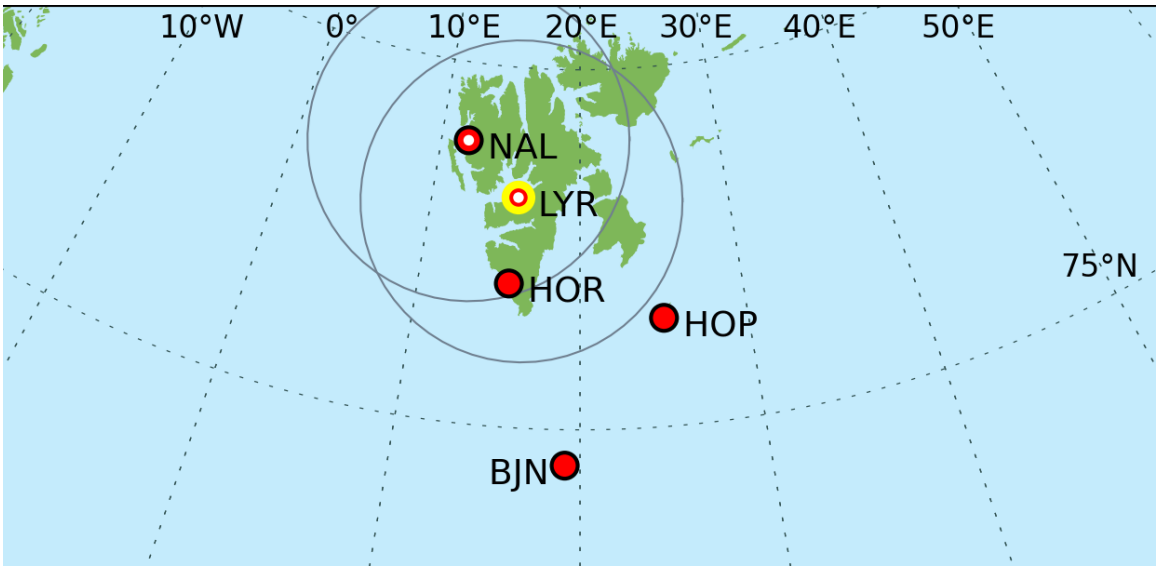

Figure 4.2: Field of view of ASC in Longyearbyen and Ny-Ålesund [FMI].

Figure 4.2 shows, with grey circles, the overlapping field of views of the LYR and NAL cameras. Auroral structures will therefore often be observed at both stations at the same time. If the auroral oval is located at lower latitudes, the aurora may be seen south of Longyearbyen, but not at all in the field of view of the Ny-Ålesund camera. The figure also displays the instruments present at each station. The red dots at Hopen (HOP), Bjørnøya (BJN) and Hornsund (HOR) indicates that the stations have magnetometers. The red and white dot at Ny-Ålesund (NAL) represents both magnetometer and all-sky camera. The yellow, red and white dot at Longyearbyen (LYR) indicates the presence of magnetometer, all-sky camera and GPS receivers.

4.1.2 Advanced Composition Explorer (ACE)

The spacecraft ACE (figure 4.3) is situated at the first Lagrange point between the Sun and Earth, situated at 1,5 millions kilometers from the Earth towards the Sun. A Lagrange point refers to locations in space where there is a stability between a spacecraft's, Sun's and Earth's orbital motion and gravitational forces. These stable conditions allow measurements to be made. ACE measures the propagation of the

solar wind towards Earth and its parameters (velocity, pressure and particle density) and also the interplanetary magnetic field with its magnetometer with a one minute time resolution. The time used by the solar wind to propagate towards the magnetopause varies with its velocity. For an average solar wind velocity of 400 km/s, the propagation time from the moment it is detected by ACE until it reaches the magnetopause is around one hour.

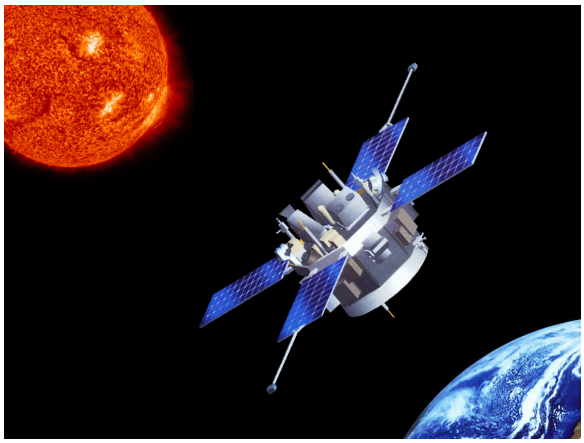

Figure 4.3: Artist's rendition of the ACE spacecraft observing the Sun [NASA].

4.2 Arciness index

The arciness index was derived by Whiter et al. (2013) in order to obtain an automated algorithm permitting the the quantification of the auroral structures observed by All-Sky Cameras. The index varies from 0 to 1 and describes how much the observed auroral structures resembles arcs. This will provide information about the presence of different auroral forms in different sections of the day related to the interaction between the solar wind and the magnetosphere-ionosphere system [Partamies et al., 2014]. The arciness index may also give an understanding of the coupling processes between the magnetosphere and the ionosphere. Arcs result from field aligned currents flowing through the ionosphere creating auroral electrojets. Figures 4.4, 4.5 and 4.6 show all-sky-images for arciness equal to 1 (the dominant auroral structure is an arc), 0.7 (medium arciness, often corresponding to more complex auroral structures) and 0.5 (low arciness) respectively.

The all-sky camera images are first sorted into two classes of "no aurora" and "aurora" based on the number of pixels above a certain brightness threshold is large enough, the image is considered containing aurora. The Moon and broken clouds can be seen as bright objects that might be mistaken for aurora. The image is classified as "no aurora" if the Moon is the only bright structure in the picture as the brightness would be considered arciness. If the sky is overcast, no discrete auroral structures are observable and these images will also be discarded [Syrjäsuo, 2001]. This analysis uses paired data thus, any auroral observations from one single station will not be considered. Furthermore, images within five minutes of UT midnight, rarely containing aurora, images for where the Sun is above the horizon and images that do not have a paired image from another station at the same time will not be considered for arciness analysis [Partamies et al., 2014].

As briefly mentioned in the description of the MIRACLE network, the LYR and NAL all-sky cameras have overlapping field of views. However, the same auroral structures are not always observed at both stations at the same time and structures seen as arcs (A=1) in Ny-Ålesund may appear as complex structures (smaller arciness index) over Longyearbyen, or vice versa. This is pictured by two examples in figure 4.7. The two top drawings show the same arc (A = 1) observed in LYR (left) and in NAL (right) at the same time. The arc is situated further south in the NAL field of view due to the station being located further north of the auroral oval than LYR. In the bottom right drawing, the arc observed in the NAL field of view (bottom left drawing) is no

longer seen as an arc in the LYR field of view and will therefore be considered as a more complex auroral structure (A = 0.8).

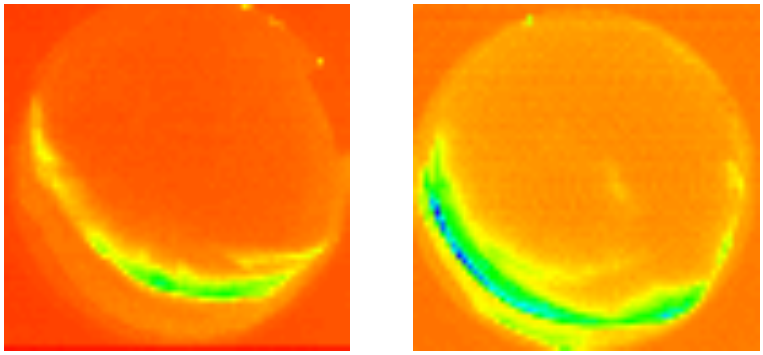

(a) Daytime aurora 22/12/2003 12:18:00 UT.

(b) Nighttime aurora 22/12/2003 17:24:00 UT.

Figure 4.4: ASC images showing arciness index equal to 1.

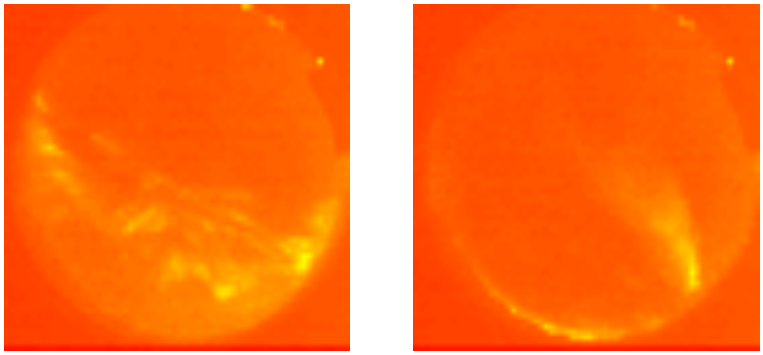

(a) Daytime aurora 22/12/2003 09:39:00 UT.

(b) Nighttime aurora 22/12/2003 16:19:00 UT.

Figure 4.5: ASC images showing arciness index equal to 0.7.

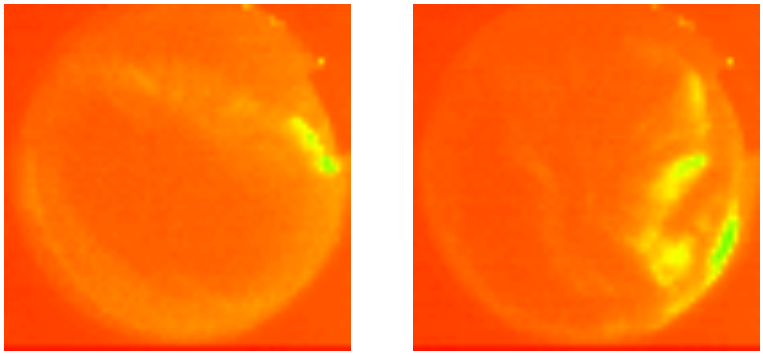

(a) Daytime aurora 24/12/2003 11:37:00 UT.

(b) Nighttime aurora 22/12/2003 18:04:00 UT.

Figure 4.6: ASC images showing arciness index equal to 0.5.

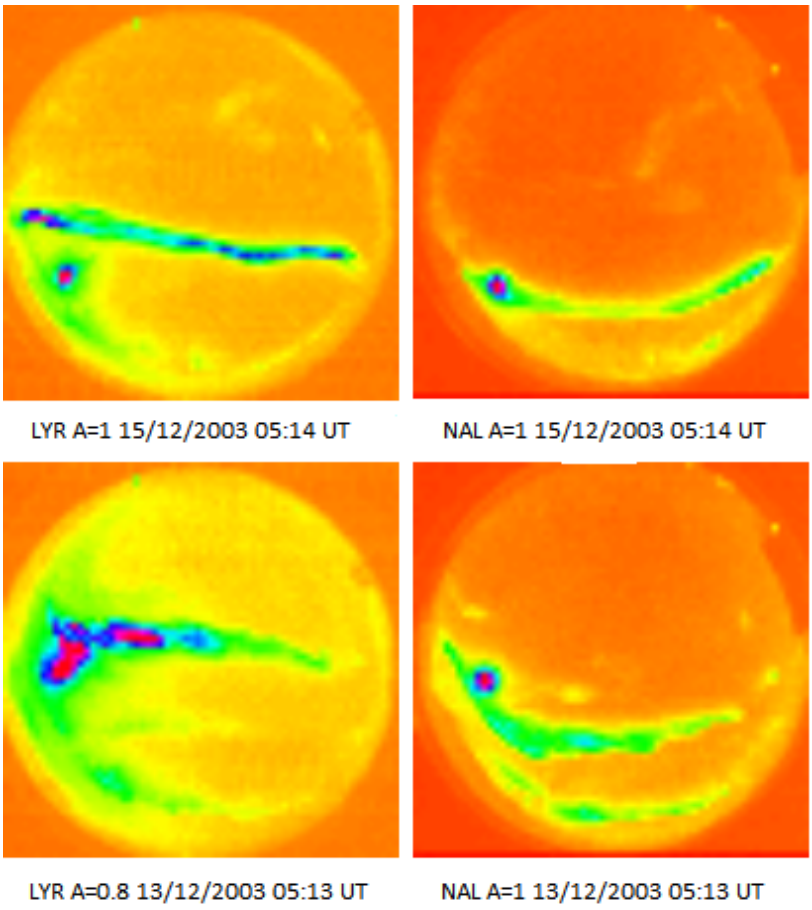

Figure 4.7: ASC images of arcs observed over Longyearbyen and Ny-Ålesund.

The data from both stations is coupled which means that structures are considered as aurora if they are detectable in both field of views. If one station observes clouds or has technical difficulties (for example data gaps when the auroral observatory in Longyearbyen was moved from Adventdalen to Breinosa), the structures observed simultaneously by the other station will not be considered.

The calculation of auroral arciness index was derived from the study of Whiter et al., 2013 on a new automated algorithm to estimate the peak auroral emission height from all-sky camera images.
Each all-sky camera image is binned to 128 $\times$ 128 pixels which corresponds an average spatial resolution of two kilometers at ionospheric heights. The median pixel value in corners outside the circular field of view is not counted in order to remove the dark current contribution to all pixels. The pixels above a brightness threshold are then grouped into clusters so that all pixels in one cluster are adjacent to another pixel in the same cluster. Bright pixels appearing far from another bright pixel are

neglected. The brightness varies on a scale from 0 to 255 (8bit scale) with a typical value of 120 if there are more than 1000 pixels above this value. If the amount of pixels are insufficient (below 1000), the threshold value will be lowered until more than 1000 pixels are above this threshold. The brightness threshold can not be any lower than 8 which is just above the dark-corrected intensity of clear and dark skies [Partamies et al., 2014].

The clusters of adjacent pixels need to contain more than 20 pixels in ordered to be considered independent structures. Smaller clusters will be ignored. Each independent structure is fitted to a polynomial of the order of $log_{10}(n)$, with n being the number of pixels in the structure. The higher the number of pixels in the cluster is, the higher will the degree of order of the polynomial fit be. The error of each fit is described by the chi-squared goodness of fit, χ^2. The sum of all χ^2 for all clusters is then normalized to the total number of pixels in the structure (n) in order to describe the distribution of bright pixels with respect to the polynomial fit line (M) [Partamies et al., 2014].

$$M = \frac{\Sigma\chi^2}{\Sigma n} \tag{4.1}$$

Equation 4.1 depends on the wideness of the auroral structure as the pixels are located further away from the $log_{10}(n)$ fit line. Wide structures will result in higher M-values. Figure 4.4a show a dayside arc which corresponds to an arciness index of 1. The arc is a slim structure and elongated in the dawn-dusk plane. This shape is a good approximation to the polynomial fit line which results in low χ^2 and thus a small M. Figure 4.6b show complex nightside auroral structures. These structures are wider and will therefore be a poor fit to the polynomial fit line. The χ^2-values are elevated and will result in a higher M-value.

The weighted number of structures is defined as:

$$N = [\Sigma(\frac{n}{\Sigma n})^c]^{-\frac{1}{c}}, \tag{4.2}$$

where c is the number of structures and the summation is over all independent structures in one image. The most dominant structure is the structure containing the largest number of pixels. Looking at figure 4.4a, all bright pixels are gathered in one structure. Equation 4.2 will therefore result in N=1 since there is only one independent structures (c=1). In the case of Figure 4.6b, there are multiple independent

structures. The weighing number c is greater than one and the summation and normalisation of all pixels of each structure separately and all structures together result in an elevated value (>1) for N. The more independent structures in one image, the higher the N-value will be.

The arciness index A is then defined by:

$$A = min[\frac{3.0}{ln(NM)}, 1.0] \tag{4.3}$$

A ranges from 0 to 1 with A=1 meaning that the dominant structure in the all-sky image is an arc. The minimum function (min) inserted in equation 4.3 ensures that no auroral structure gets defined with a higher arciness index than 1. For each image, the arciness index decreases with an increasing number of independent structures (larger c in equation 4.2) or if χ^2 is large compared to total number of independent structures (larger M in equation 4.1) because the polynomial fit becomes poorer [Partamies et al., 2014]. Figure 4.4a corresponds to A=1 as the image consists of one single bright and slim structure that will follow the $log_{10}(n)$ polynomial fit well. Figure 4.6b, on the other hand, has at least four independent bright structures with a rather wide shape. Their approximation into the fit line will be poor (defined by errors) and the arciness index will be low.

In order to be able to observe clear auroral structures, only the green line (557.7 nm) has been considered. From 2000 to 2012, 184644 images were classified as green aurora with calculated arciness index from LYR and 174788 images from NAL.

Two studies have previously been made using the arciness index for nighttime observations over Fenno-scandia. The first study by Partamies et al. (2014) describes the approach of the algorithm leading to the calculation of the arciness index, as described above, and applies it to determine the correlation between the solar cycle and diurnal variations and auroral structures. A total of one million images from five all-sky cameras from stations in northern Finland and Sweden (MIRACLE) have been analysed and assigned arciness indexes. The data sets are ranging over solar cycle 23, from 1996 to 2007. The arciness data was binned into A=1 corresponding to arcs and A<0.9 corresponding to complex auroral structures. The analysis resulted in an agreement with previous studies made in determining the diurnal evolution of the aurora. By looking at all-sky camera images for several events and comparing to images of situations with arciness index equal to one, it was validated that the clearest auroral arcs correspond to A=1. By studying the diurnal variation of the

arciness, arcs were observed throughout the night, but occur most frequently in the evening and premidnight and least in the early morning hours. The arcs observed premidnight will evolve into more complex and broken forms in the postmidninght and morning sectors. Also, the study shows a cyclic auroral behaviour over the solar cycle. Arc-like structures are more present during quiet magnetic years (years with fewer sun spots) than when approaching solar maximum. However, there is a difference in the correlation between quiet arcs (A=1) and more complex structures (A<0.9) with the solar cycle. The occurrence of more complex auroral structures is better correlated to the solar cycle than the quiet arcs suggesting that dynamic aurora is more directly driven by the geomagnetic activity without having much effect on the occurrence of quiet auroral arcs [Partamies et al., 2014].

In the second study, Partamies et al. (2015) utilizes the same data sets as in the previous study to determine the structure of the aurora resulting from substorms. The substorms and their phases are identified by IMF data and ground magnetometer data. Growth, expansion and recovery phases were detected and compared to arciness data. Within these three phases, around $\frac{1}{3}$ of all auroral structures were determined to be cases with A=1 (arcs), except for cases of very high K_p indexes (quantification of the geomagnetic disturbances on a scale from 0 to 9) where the auroral oval is situated further south (out of the field of view of the cameras). K_p=3 is the best condition to observe arcs in northern Scandinavia and northern Finland. The dawn sector (05.00 to 10.00 MLT) has the least amount of arcs and the premidnight sector (16.00 to 21.00 MLT) contain the highest concentration of arcs. The study also shows that the substorm growth phases have the longest arc-dominated periods and also arcs with the longest lifetime. The expansion phases has the longest arc waiting time (time separation between the end of an arc event and the beginning of a new one) and the shortest arc lifetime. The analysis also suggests that the substorm growth phase starts a few minutes before aurora is observed from the time gap between the beginning of the magnetospheric substorm growth phase and the first obtained arciness index [Partamies et al., 2015].

Chapter 5

Results

Data from All-Sky Cameras in Longyearbyen (LYR) and Ny-Ålesund (NAL) from 2000 to 2012 have been compared to solar wind parameters (magnetic field components and strength of IMF, and velocity) from the ACE spacecraft. The goal of the study is to establish correlations between the structures in the dayside aurora, as determined by the arciness index, and the incoming solar wind and IMF.

The solar wind, with the frozen-in IMF, streaming through the heliosphere will be detected by the ACE spacecraft when approaching the near Earth Space environment. In this analysis, the IMF B_z and B_y components have been binned according to magnitude (only B_z) and polarity and then compared to corresponding values for arciness. The comparison of solar wind data from ACE with arciness data from ASC is done by pairing the date and time of the observed aurora with the corresponding time for solar wind data. As discussed in the previous sections, the IMF B_z and B_y components decide where in the magnetopause the reconnection will take place and therefore also play a role in how the solar wind particles are transferred to the upper atmosphere and the motion of any auroral structures. The dayside auroral activity observed over Svalbard has also been compared to variations in the solar wind velocity. Whilst an exact correlation between dayside auroral activity and solar wind velocity has not been found it can often be used as a proxy for turbulence in the dayside magnetosheath (e.g. Dimmock et al.(2014)). One logical conclusion from increased turbulence could be increasingly chaotic auroral activity as the very nature of the magnetosphere-ionosphere system is that of a coupled system. Additionally, increases in solar wind dynamic pressure (which is dependent on solar wind velocity, c.f equation 2.18) have been linked to changes in the dayside reconnection rate, which would in turn influence the location of such features of cusp aurora. On a larger scale, as the

geomagnetic activity increases, the auroral oval vary in size and location on both the day-and nightside. The oval broadens and expands poleward and equatorward, but to a much larger extent on the nightside than on the dayside [Feldstein and Starkov, 1967].

In this chapter occurrences from different events are observed. An event is a gathering of single occurrences over a longer time span which, in this study, corresponds to one day worth of observations.

5.1 Binning the data

Between 2000 and 2012, thousands of auroral arc-like structures have been observed by the ASC in Longyearbyen and Ny-Ålesund. For the purposes of this study, the data sets have been limited to strictly dayside times (including the cusp region times) between 09.00 and 14.00 MLT which corresponds to 06.00-11.00 UT at Svalbard latitudes. The dayside arciness data were then paired to the IMF B_z-component. The polarity of this component decides if there will be a reconnection at the magnetopause ($B_z < 0$) or in the tail lobes ($B_z > 0$). Different auroral forms are expected to be observed for opposite IMF B_z polarities, as discussed in section 3.3. The data was then divided into four bins depending on both polarity and magnitude: -10 nT $\leq B_z <$ -5 nT, -5 nT $\leq B_z <$ 0 nT, 0 nT $< B_z \leq$ 5 nT and 5 nT $< B_z \leq$ 10 nT. Furthermore, each of these four bins were divided into two new bins depending on the polarity of the IMF B_y-component ($B_y <$0 nT and $B_y >$0 nT). Eight bins are therefore considered in the analysis, here listed in Table 5.1 with the number of data points contained in each bin and the number of events these data points originate from.

The polarity of the IMF B_y-component determines the inclination the IMF and therefore plays a role in the location of the reconnection point. If $B_y >$0 nT, the reconnection in the magnetopause will be skewed towards dawn, and towards dusk if $B_y <$0 nT. Thus the location of the cusp will be shifted towards dusk or dawn, respectively, depending upon the By polarity.

In general, average IMF B_z magnitudes range between 0 and 5 nT at 1 AU [Prölss, 2004], which is also valid for the data presented here. A significant amount of data points (around ten times more than bins of higher magnitudes) will be grouped into four bins with 0 nT$< \mid B \mid \leq$ 5nT and varying B_z and B_y polarities. The bins

Table 5.1: Listing of bins depending on IMF B_z magnitude and orientation and B_y polarity for arciness observations over Longyearbyen and Ny-Ålesund. The number of data points and events contained in each bin for each station is also precised in the four last columns.

		Longyearbyen		Ny-Ålesund	
B_z [nT]	B_y [nT]	Datapoints	Events	Datapoints	Events
$-10 \leq B_z < -5$	< 0	157	23	155	21
$-5 \leq B_z < 0$	< 0	1136	94	1107	91
$0 < B_z \leq 5$	< 0	1130	104	1090	87
$5 < B_z \leq 10$	< 0	144	17	143	15
$-10 \leq B_z < -5$	> 0	132	19	130	23
$-5 \leq B_z < 0$	> 0	1464	78	1405	75
$0 < B_z \leq 5$	> 0	1170	71	1117	69
$5 < B_z \leq 10$	> 0	131	16	124	15

containing a large amount of data points divided over multiple events have a larger statistical weight than bins with smaller amount of data points derived from few events. The solar wind velocity has also been compared to the arciness data. The velocity data was binned into six bins depending on strength. The variation in velocity was compared to the corresponding arciness data for all IMF conditions. A focus was also made on comparing the arciness index to magnetic local time for the same velocity bins (listed in Table 5.2) when IMF B_z <0 nT.

Table 5.2: Listing of velocity bins for both IMF B_z orientations and for B_z <0 explicitly for arciness observations over Longyearbyen and Ny-Ålesund. The number of data points and events in contained in each bin for each station is also precised in the four last columns.

		Longyearbyen		Ny-Ålesund	
Solar Wind Velocity [km/s]	B_z [nT]	Datapoints	Events	Datapoints	Events
$v < 400$	All	788	43	700	43
$400 \leq v < 500$	All	964	53	925	51
$500 \leq v < 600$	All	1449	42	1434	42
$600 \leq v < 700$	All	1491	34	1436	43
$700 \leq v < 800$	All	556	10	555	10
$v \geq 800$	All	48	4	48	4
$v < 400$	< 0	540	39	497	35
$400 \leq v < 500$	< 0	406	35	395	38
$500 \leq v < 600$	< 0	702	33	698	32
$600 \leq v < 700$	< 0	732	30	700	27
$700 \leq v < 800$	< 0	364	8	363	8
$v \geq 800$	< 0	20	4	20	4

The two types of instrumentation used in the study (ACE and ASCs) have different temporal resolutions, which make a direct pairing of the data challenging. The solar

wind parameters (measured by ACE) have a temporal resolution of 60 seconds, whilst the ASC data have a temporal resolution of 20 seconds. To avoid duplication of data points, the arciness index data was only utilized at a 60 second temporal resolution (i.e. every third data point in a continuous time series).

In order to gain an understanding of the temporal evolution of the arcs and auroral structures, the arciness data has been plotted in two different manners:

- Histograms with arciness occurrences as a function of magnetic local time. The arciness indexes were grouped into A=1 (arcs) and A $\leq$ 0.9 (complex auroral structures) for each bin. The arciness indexes ranging between 0.9 and 1 (0.9<A<1) represent a "transition zone" between pure arcs and more complex signatures. The occurrences for this region were not used in the analysis to ensure a better distinctions between the time evolution of arcs and complex structures. This bin is also ignored for the same reasons in the study of Partamies et al.(2014).
- Scatter plots of arciness index as a function of magnetic local time. A first degree polynomial fit was then made to facilitate the comparison between the different stations and bins.

The study here will build upon the previous study by Partamies et al.(2014), which studied the arciness of structures on the nightside. It will also aim to quantitatively characterize the auroral features such as arcs (A=1) and auroral structures (A<0.9) in the both the pre-and postnoon sectors, but mainly within the cusp region.

5.2 Evolution of dayside aurora from 09.00 to 14.00 MLT

The distributions were examined in the first instance for any obvious features which could be attributed to the polarity of the IMF B_z component. It was found that the arciness distribution as a function of MLT for both IMF -5nT$\leq B_z <$0nT and IMF 0nT$< B_z \leq$5nT were statistically similar. One explanation for this could be due to the fact that, if, during an event the B_z component is fluctuating about 0 (which is often the case) data from an 'event' will be split between the two distributions (B_z >0 and B_z <0), resulting in two similar distributions. As such this analysis focuses on looking at 1) B_y effects during B_z >0 and 2) B_y effects during strongly B_z negative

(-10nT$\leq B_z <$-5nT). When examining these two cases, instances where this 'event splitting' occurs are removed. In this section, the study will focus on differences between B_y polarities for 0nT$<B_z\leq$5nT.

The temporal evolution of the dayside aurora is studied by grouping arcs and complex structures separately. In figure 5.1 and 5.2, the arciness A is divided into two bins: A<0.9 and A=1. A<0.9 is defined as complex auroral structures and A=1 corresponds to simple or multiple arcs, as explained in the previous section. The histograms show the occurrence of the arciness bin as a function of MLT when the IMF in this case is pointing northward with a magnitude of the B_z-component ranging from 0 to 5 nT and both polarities of B_y are considered.

Considering the case with $B_y >$0, figure 5.1b shows a high amount of cases with A<0.9 between 09.00 and 10.30 MLT which corresponds to more complex auroral structures. In figure 5.1d, there is a grouping of arcs in the post-noon MLT sector.

Figures 5.1a and 5.1c are also representing arciness indexes for positive IMF B_z-components, but negative IMF B_y. The figures show the same trends as their corresponding arciness bin for IMF B_y positive.

Since the field of view for the ASC in Ny-Ålesund is overlapping with the ASC field of view in Longyearbyen, it is expected to observe similar signatures and trends of the time distribution of the aurora at both stations. However, as already discussed in Chapter 4, auroral forms observed as arcs by the ASC at one station may not be captured as full arcs at the other station, but rather as arc-like structures with lower arciness index values.

By comparing the histograms representing the arciness data in Ny-Ålesund, figure 5.2, with their corresponding ones from Longyearbyen in figure 5.1, it is evident that the number of data points is more than doubled in Longyearbyen. Nevertheless, table 5.1, states that the number of data points are close to equal at both stations. This difference in number of data points observed in the histograms might be due to them being within the $0,9 <$A<1 bin. Looking at figure 5.1a, figure 5.1b, figure 5.2a and figure 5.2b, they all show an increase of complex auroral structures (A<0.9) in the mid-morning sector (09.00 to 10.00 MLT). Figure 5.1c and figure 5.1d, also show higher amounts of data points from 09.00 to 10.00 MLT, meaning that the mid-morning sector is populated by auroral arcs (A=1). These are also observed in the postnoon sector (13.00-14.00 MLT). The mid-morning auroral arcs are also observed over Ny-Ålesund as shown in Figure 5.2c and Figure 5.2d. Both arcs and complex

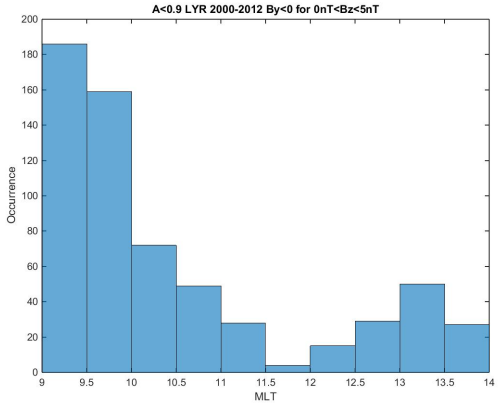

(a) A<0,9 for 0< B_z <5 nT and B_y <0.

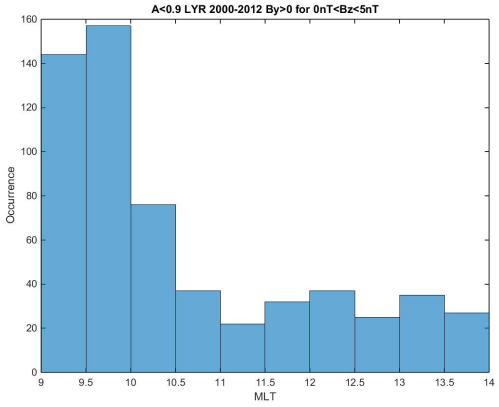

(b) A<0,9 for 0< B_z <5 nT and B_y > 0.

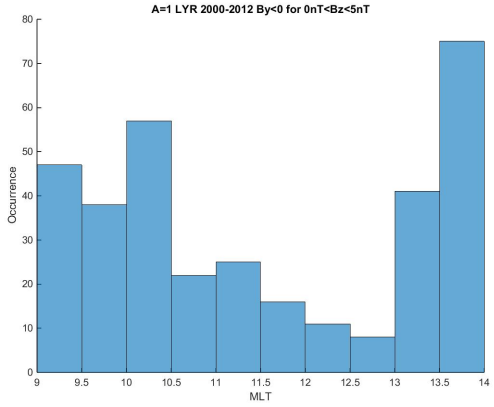

(c) A=1 for 0< B_z <5 nT and B_y < 0.

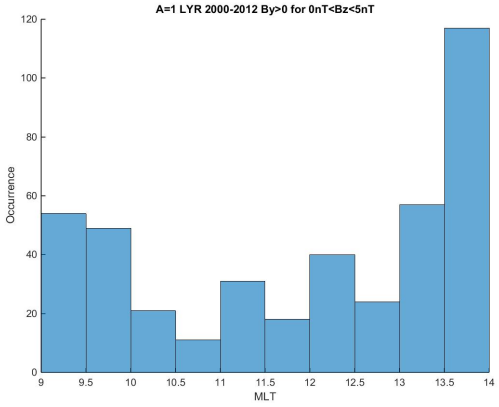

(d) A=1 for 0< B_z <5 nT and B_y > 0.

Figure 5.1: Longyearbyen Occurrences over Magnetic Local Time of arcs and complex auroral structures depending on the polarity of B_y for 0< B_z <5 nT

structures are less present in the midday sector (11.00-13.00 MLT). This is called the "midday gap" and is manifested by the absence of extended, discrete auroral arcs in the midday sector of the auroral oval [Dandekar and Pike, 1978]. Since the IMF B_z is positive, the reconnection will occur in the tail lobes and not in the sub-solar point. There is therefore no direct entry point for solar wind particles into the ionosphere (i.e. no direct cusp signatures).

By comparing the histograms with opposite B_y polarity to each other, it can be seen that the overall distribution of arcs (A=1) and auroral structures (A<0.9) does not change dramatically under B_z >0. The largest occurrences still tend to occur at earlier or later MLTs. The most noticable difference appears to be an increase of occurrences around midday for B_y >0. This is particularly evident when comparing figures 5.2a and 5.2b (complex structures, A<0.9).

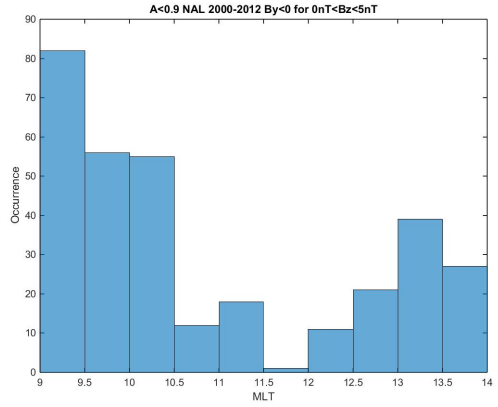

(a) A<0,9 for 0< B_z <5 nT and $B_y < 0$.

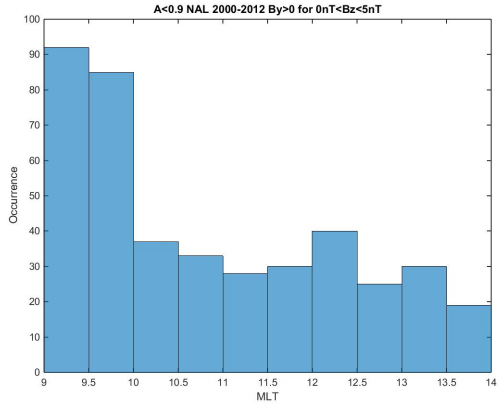

(b) A<0,9 for 0< B_z <5 nT and $B_y > 0$.

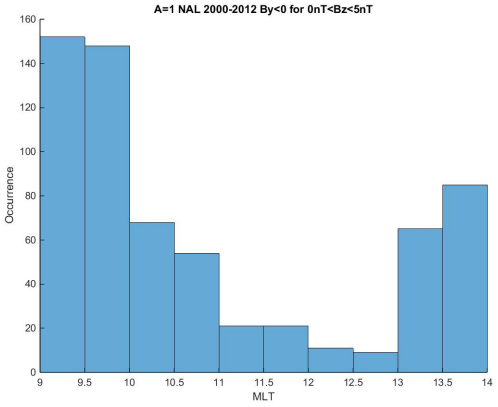

(c) A=1 for 0< B_z <5 nT and $B_y < 0$.

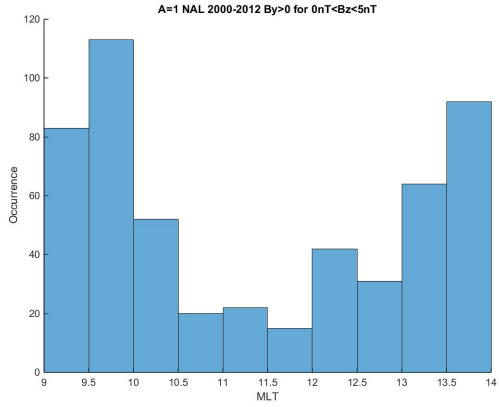

(d) A=1 for 0< B_z <5 nT and $B_y > 0$.

Figure 5.2: Ny-Ålesund Occurrences over Magnetic Local Time of arcs and complex auroral structures depending on the polarity of B_y for 0< B_z <5 nT

Reconnection between IMF $B_z > 0$ and the geomagnetic field occurs in the open tail lobes in the high-latitude magnetopause tailward of the cusp [Dungey, 1963]. The plasma at the footprint of the reconnection X-line convects sunward, due to magnetic tension of the newly reconnected field lines, before being swept anti-sunward towards dawn and dusk with the magnetosheath flow [Chisham et al., 2004]. As illustrated in the bottom middle panel of figure 2.7, this type of reconnection drives a four-cell convection with two reversed convection cells (merging/lobe cells) within the polar cap and two elongated cells of with "normal" oriented plasma convection (viscous cells) at lower latitudes driven by the viscous processes at the magnetopause [Cumnock et al., 1995]. As the newly opened field lines convect sunward following reconnection, particles precipitate at different latitudes [Onsager et al., 2001].

By studying the auroral dynamics for a northward IMF B_z-component and see how the structures evolve with different IMF B_y polarities, the location of the precipitation

regions for a four-celled convection pattern can be connected to the observed auroral forms.

5.3 Dependence on B_y polarity when -10< B_z <-5 nT

5.3.1 Arc occurrence

Magnetopause reconnection occur when a southward directed z-component of the IMF merges with the geomagnetic field. The polarity of the B_y-component decides the inclination of the IMF and thus, that the reconnection point will be shifted towards dawn for positive B_y and dusk for negative B_y. The study in this section focuses on strong IMF B_z magnitudes (compared to the ones for B_y) in order to ensure a stable subsolar reconnection. By comparing the histograms of occurrence of arciness A = 1 and A < 0,9 separately as a function of MLT when -10 < B_z < -5 nT for both B_y polarities, the effect of the different B_y polarities on the auroral forms may reveal the type of dayside aurora and thus their originating precipitation region.

Figure 5.3 shows the time distribution of occurrences of arcs and auroral structures observed in Ny Ålesund when the IMF B_z-component is ranging from -10 to -5 nT and the B_y polarity is either positive or negative. This part of the study will only be based on observations from Ny-Ålesund as they agree with the corresponding histograms for Longyearbyen. The distributions of both arcs (A=1) and auroral structures (A<0.9) differ completely for opposite B_z polarities. Since the analysis focuses on cases of strong IMF B_z <0, it is based on fewer data points than the one for B_z >0 in the previous section.

For B_y <0, arcs (A=1) as well as more complex auroral structures (A<0.9) are observed prenoon (09.00-11.00 MLT). Complex structures (A<0.9) are also present postnoon (12.30-14.00 MLT). Figure 5.3c, shows that arcs are almost exclusively present between 09.00 and 10.30 MLT.
For B_y >0, arcs are observed from 09.00 to 09.30 MLT and then from 10.30 to 14.00 MLT more evenly spread out over time. Comparing figure 5.3d with figure 5.3c, show that the change in B_y polarity introduces a population of auroral arcs (A=1) in the postnoon sector.
For B_y <0, some complex auroral structures (A<0.9) can be seen from 09.00 to 10.30

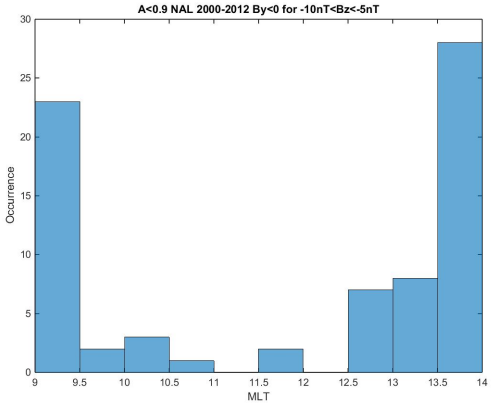

(a) A<0.9 for -10< B_z <-5 nT and $B_y < 0$.

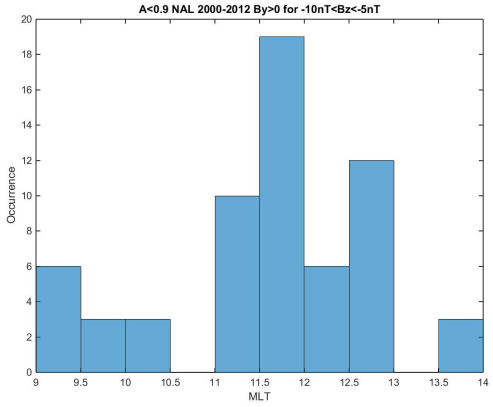

(b) A<0.9 for -10< B_z <-5 nT and $B_y > 0$.

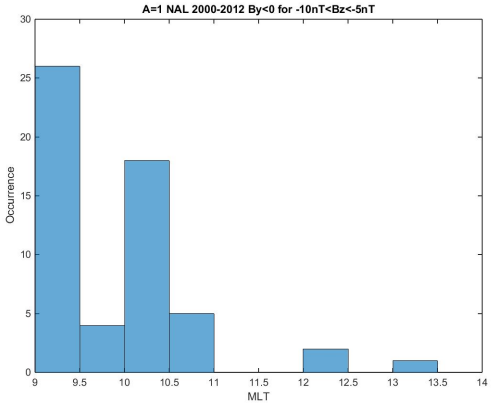

(c) A=1 for -10< B_z <-5 nT and $B_y < 0$.

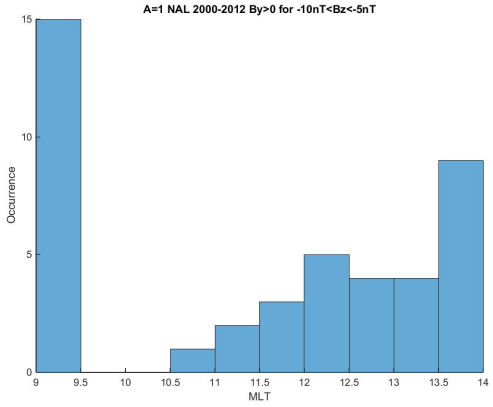

(d) A=1 for -10< B_z <-5 nT and $B_y > 0$.

Figure 5.3: Ny-Ålesund Occurrences over Magnetic Local Time of arcs and complex auroral structures depending on the polarity of B_y for -10< B_z <-5 nT

MLT and from 13.30 to 14.00 MLT (figure 5.3a).
For B_y >0, (figure 5.3b), the distribution of complex structures becomes centered at 12.00 MLT (11.00 -13.00 MLT). Comparing this to complex structures (A<0.9) when B_y <0 (figure 5.3a), the change in the B_y-polarity moves the distribution of complex structures (A<0.9) towards noon.

For negative IMF B_z-component, reconnection on the dayside will occur at the nose of the magnetopause for ideal cases of IMF B_y=0 resulting in an evenly distributed two-celled convection pattern as the one displayed on the top middle panel of figure 2.7. When including the contribution of the IMF B_y-component, the reconnection topology will be shifted towards dawn for B_y <0 and towards dusk for B_y >0 in the Northern hemisphere. This will also effect the magnetosphere-ionosphere coupling system by changing geometry of the mapping of the FAC currents in the ionosphere

altering the distribution of the plasma convection. The magnetospheric precipitation regions, mainly noticeable in the cusp region, will therefore give rise to auroral forms in different MLT sectors of the day.

5.3.2 Dayside distribution of arciness index

To get a better overview of the dayside distribution of the auroral structures, the arciness index dataset was separated into different years and plotted against magnetic local time. A first degree polynomial fit was applied to the data. The scatter plots in figure 5.4a and figure 5.4b represent arciness data for multiple years, color coded in each case according to the legend. The number of data points for each year is also indicated in the square brackets in the legend as well as the correlation coefficient. By plotting out the data in this manner it is possible to see any solar cycle effects and also observe events where 0.9<A<1 (the transition region) which are not included in figures 5.1-5.3. Comparing the trends of the scatter plots representing the time distribution of arciness indexes for different B_y polarities, observed at Ny-Ålesund, figure 5.4a shows a decrease in arcs and more complex auroral structures throughout the day for B_y <0. In figure 5.4b, there is a slight increase in arciness from 09.00 to 14.00 MLT.

In the case of a strong B_z component, the B_y polarity shows a clear impact on the increase in arciness index from 09.00 to 14.00 MLT. For a negative B_y-component, the arcs and more complex aurora (medium to high arciness) tend to be concentrated in the prenoon sector, while for B_y positive, arcs and complex structures are observable postnoon. As observed in the histograms in the previous section, arcs and auroral structures with medium to high arciness indexes (A=0.6-0.9) are present in the time span from 11.00 to 13.00 MLT. This time range has earlier been defined as a region of weak discrete aurora.

In the discussion chapter, the time distribution of the auroral structures will be linked to their corresponding auroral type in order to identify the location of their originating precipitation region for strong southward IMF B_z conditions and how the varying B_y polarities affect the magnetosphere-ionosphere coupling.

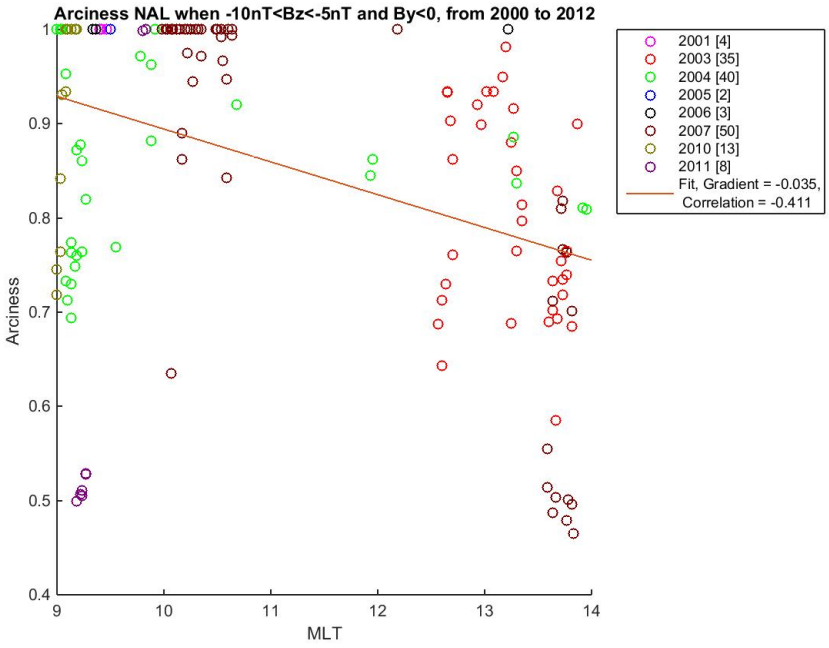

(a) -10< B_z <-5 nT and $B_y < 0$.

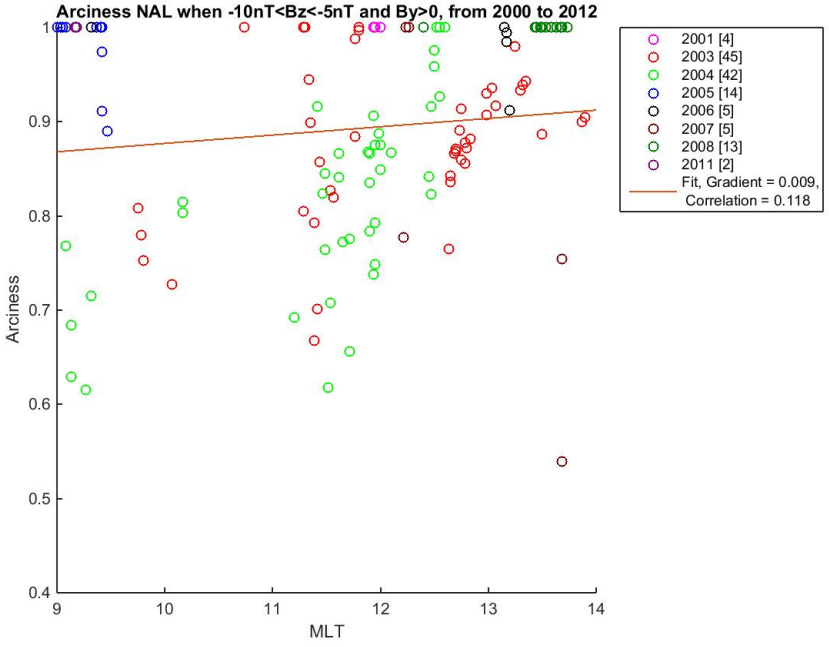

(b) -10< B_z <-5 nT and $B_y > 0$.

Figure 5.4: Ny-Ålesund Distribution of arciness indices over Magnetic Local Time depending on the polarity of B_y for -10<B_z<-5 nT

5.4 Solar wind velocity effects on the dayside aurora

5.4.1 Effects of increasing solar wind when B_z <0.

Figure 5.5 shows trends for all aurora, defined by arciness index, from 09.00 to 14.00 MLT from 2000 to 2012 when IMF B_z <0. The solar wind velocity is divided into six bins: low solar wind velocity under 400 km/s (figure 5.5a), three bins of moderate solar wind velocity, 400< v <500 km/s, 500< v <600 km/s and 600< v <700 km/s (figures 5.5b, 5.5c and 5.5d) and two bins of high velocity, 700< v <800 km/s and v >800 km/s, shown in figure 5.5e and 5.5f.

As seen from figures 5.5a-5.5e, for all velocity bins, with exception from very high velocities above 800 km/s, the arciness indexes follow the same trend with the arciness index value increasing with increasing MLT. This means that the total arciness value increases through the day which indicates a growth of arcs and auroral structures. The gradient of the trend line ranges from 0.020 to 0.042 as the velocity increases from v <400 km/s to v <800 km/s. For 600< v <700 km/s, the gradient is only of 0.004. This suggests that the variation of solar wind velocity does not affect the structuring of the dayside aurora when utilizing the arciness index. The case of slow solar wind, v <400 km/s, has a distinct signature of arcs (A=1) in the mid-morning sector (09.00-11.00 MLT). This will be discussed in more detail in the next section.

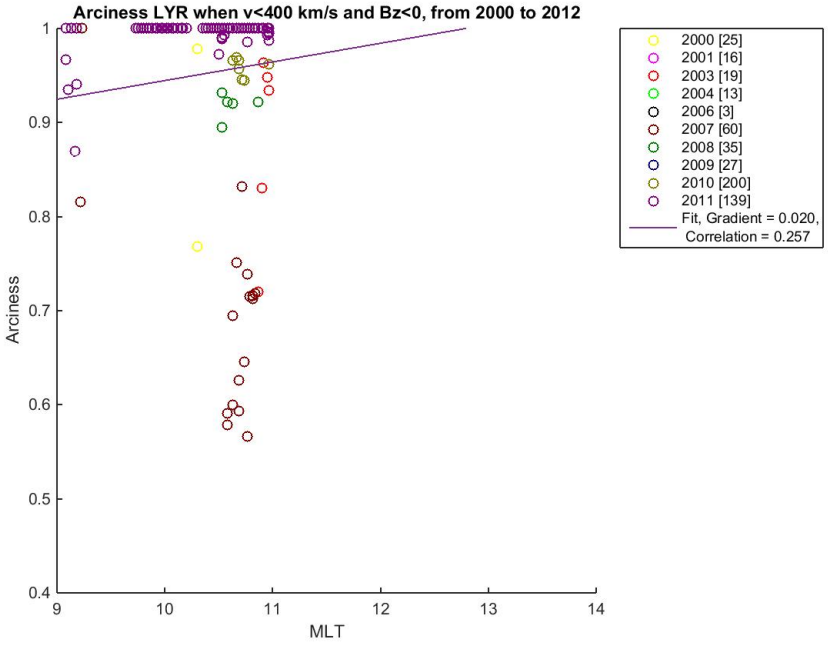

(a) v <400 km/s for $B_z < 0$.

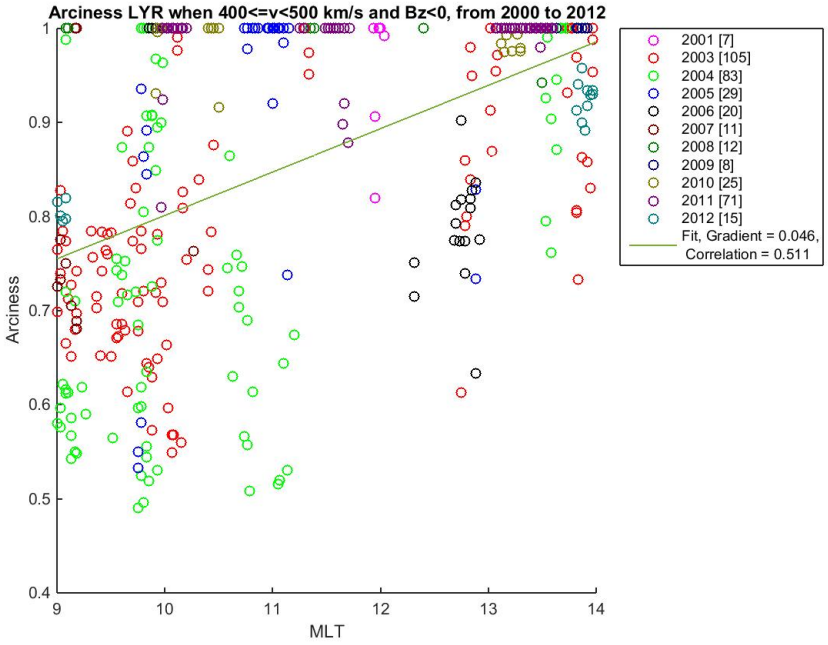

(b) 400< v <500 km/s for $B_z < 0$.

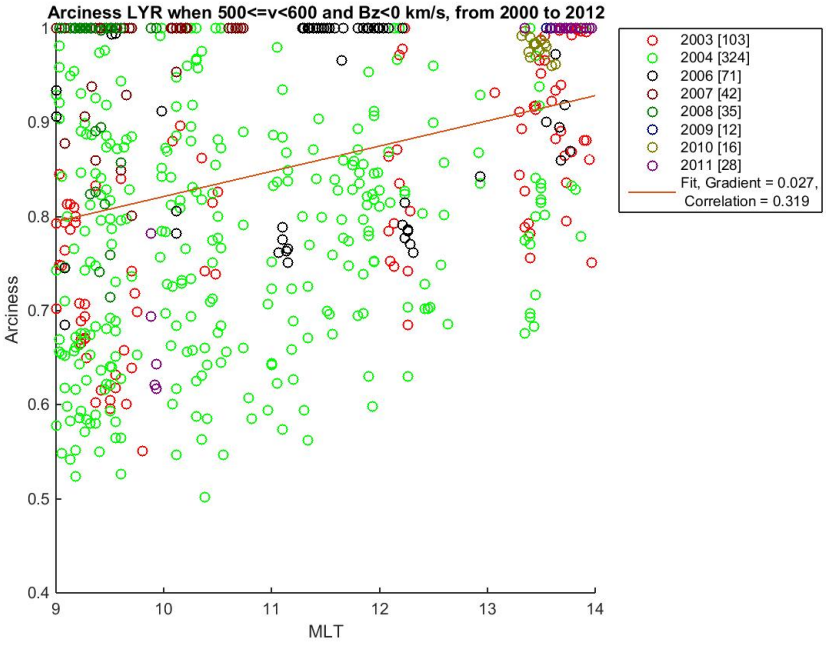

(c) 500< v <600 km/s for $B_z < 0$.

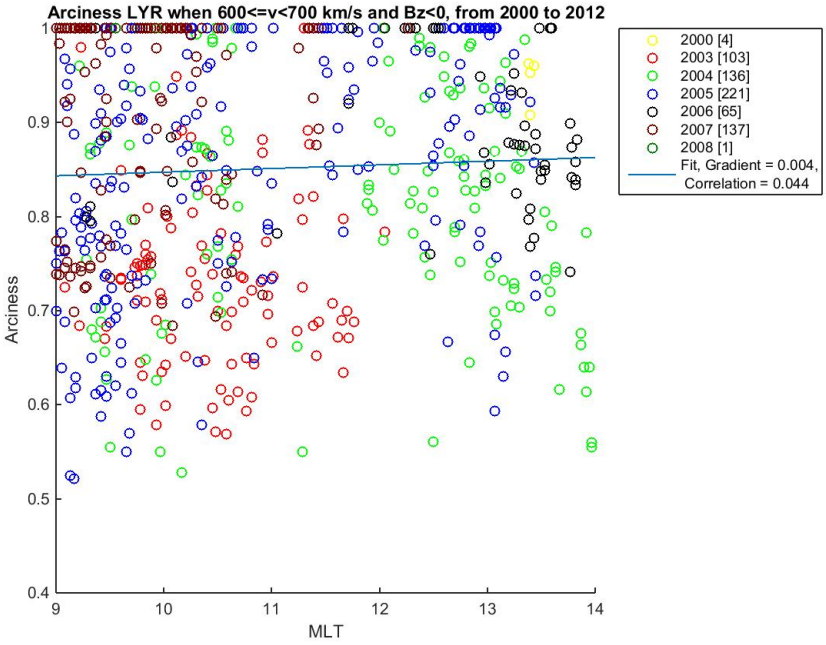

(d) 600< v <700 km/s for $B_z < 0$.

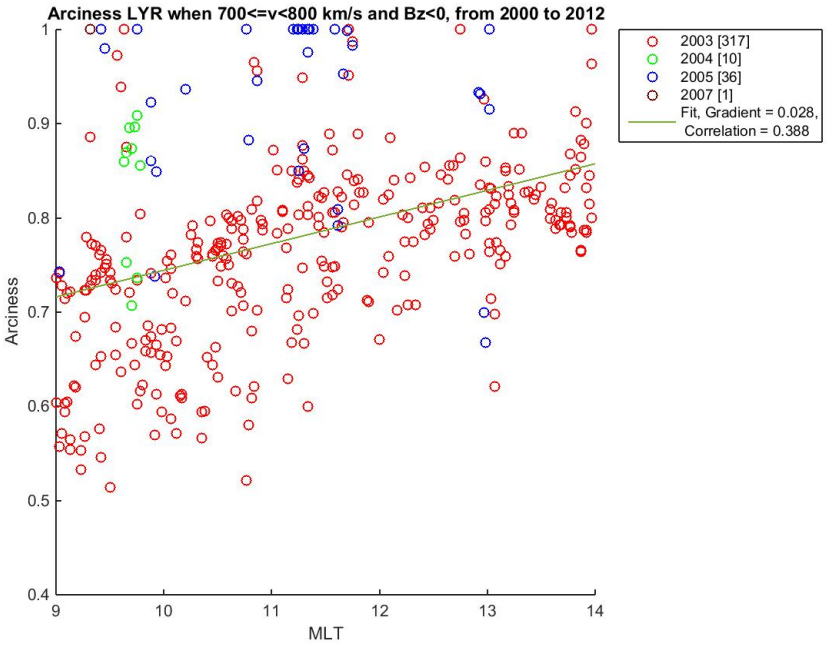

(e) 700< v <800 km/s for $B_z < 0$.

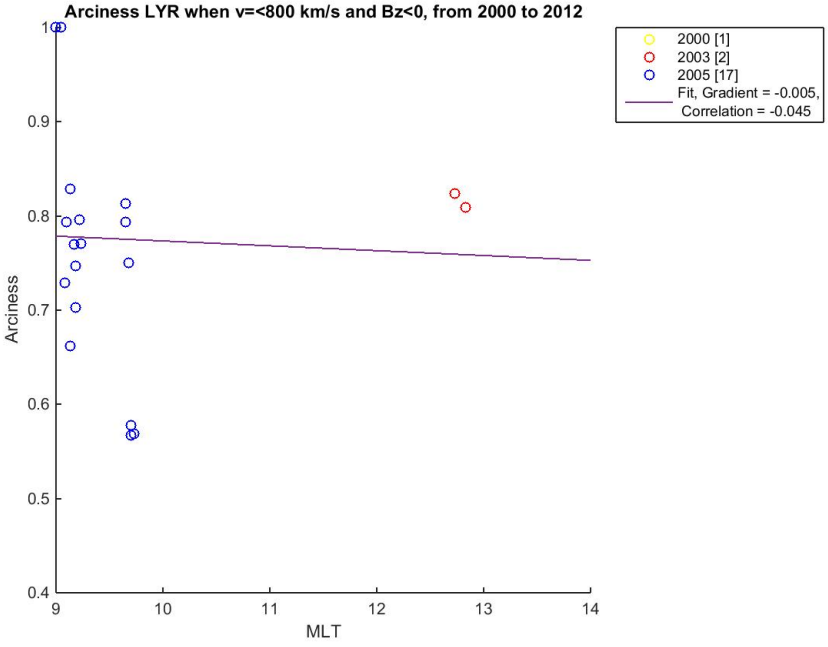

(f) v >800 km/s for $B_z < 0$.

Figure 5.5: Distribution of arciness indexes over MLT depending on solar wind velocities. Data from LYR.

5.4.2 Distribution of dayside aurora when v <400 km/s.

Figure 5.6 show the arciness indexes for the slower solar wind bin (under 400 km/s) as a function of magnetic local time, at both Longyearbyen and Ny-Ålesund stations. Figures 5.6a and 5.6c have binned the IMF B_z-component to compare with their respectively figure considering both B_z polarities (figure 5.6b and 5.6d).

Arcs (A=1) and auroral structures (A<0.9) are only observed between 09.00 and 11.00 MLT with large clusterings between 10.00 and 11.00 MLT. This same signature is also present in figures 5.7 and 5.8. The histograms represent the occurrence of arciness index equal to 1 and arciness index less than 0.9 versus magnetic local time. Arcs (A=1) are present from 09.00 to 11.00 MLT with a peak in the occurrence from 10.30 to 11.00 MLT. This is observable at both stations when IMF $B_z < 0$, but also when considering both polarities of the B_z-component (figures 5.7a, 5.8b, 5.8a and 5.8b). Complex auroral structures (A<0.9) show a similar distribution to A=1, with a peak in events between 10.30 and 11.00 MLT at both stations considering $B_z < 0$ and both B_z polarities.

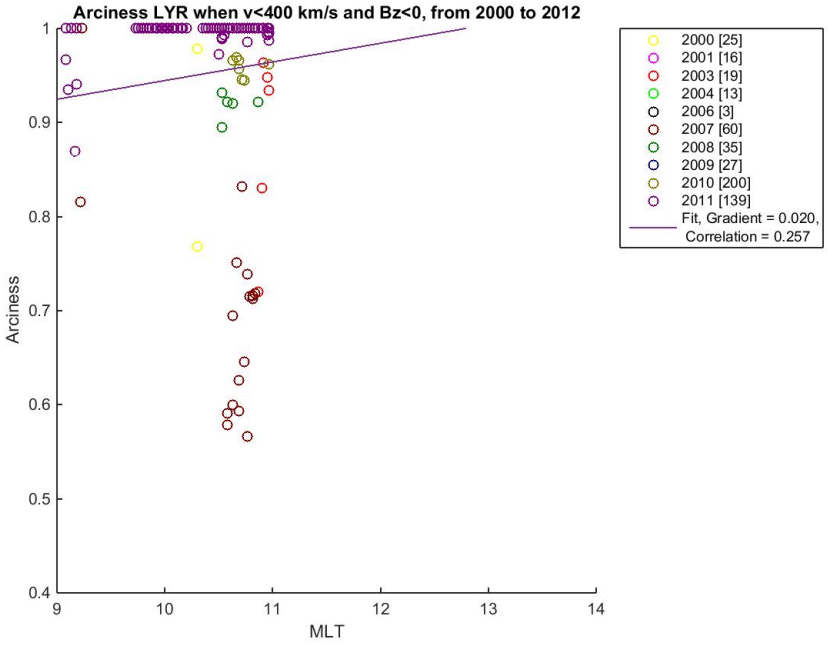

(a) LYR for $B_z < 0$.

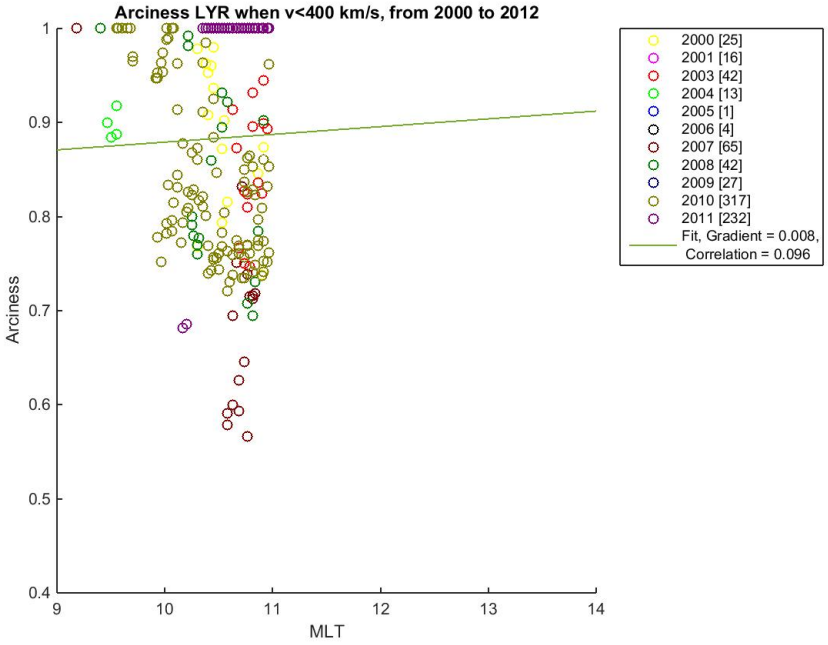

(b) LYR for both B_z polarities.

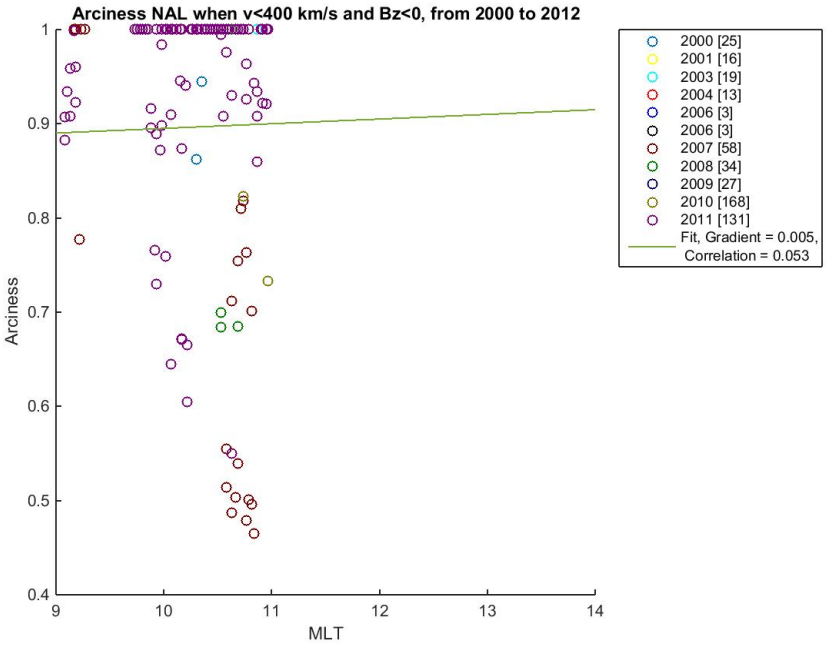

(c) NAL for $B_z < 0$.

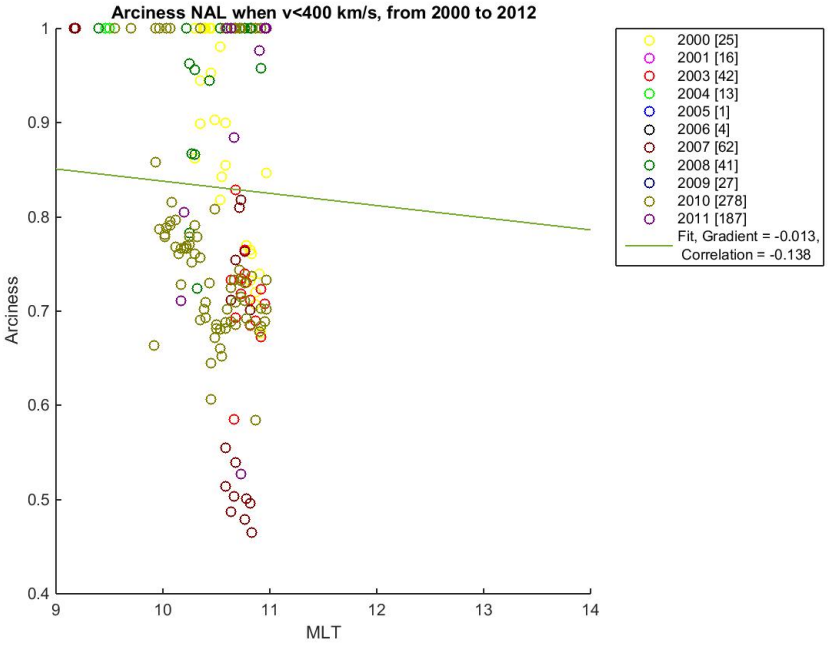

(d) NAL for both B_z polarities.

Figure 5.6: Distribution of arciness indexes over MLT when v <400 km/s.

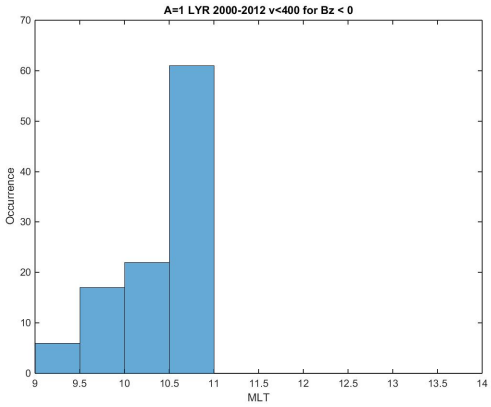

(a) A=1 LYR for $B_z < 0$.

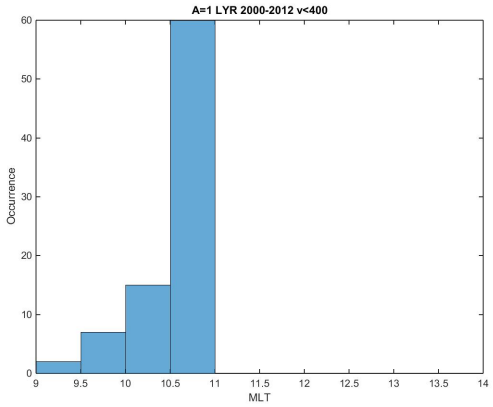

(b) A=1 LYR for both B_z polarities.

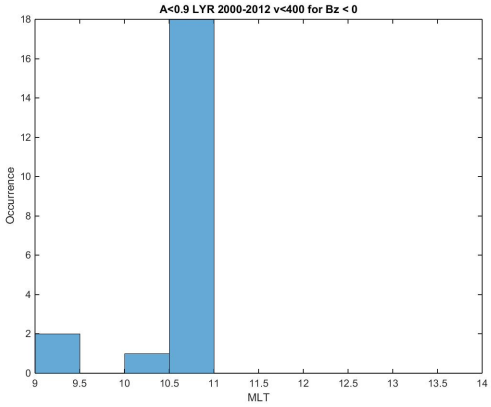

(c) A<0.9 LYR for $B_z < 0$.

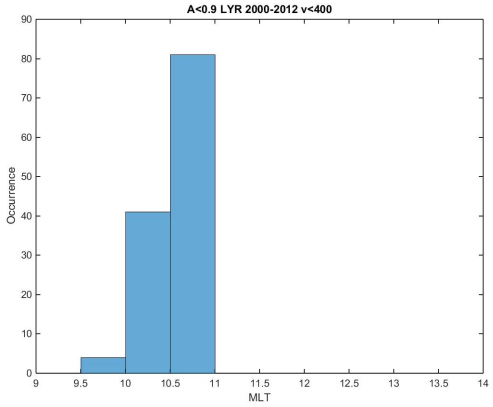

(d) A<0.9 LYR for both B_z polarities.

Figure 5.7: Occurences of arcs and complex structures observed at LYR over MLT when v <400 km/s.

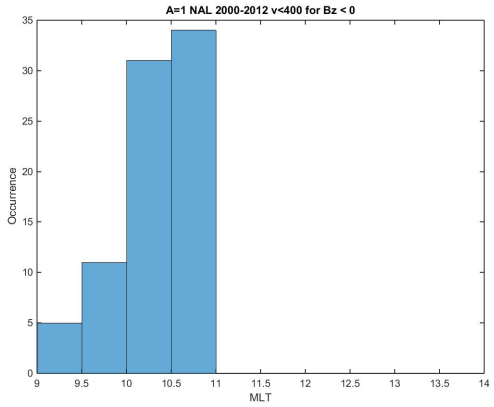

(a) A=1 NAL for $B_z < 0$.

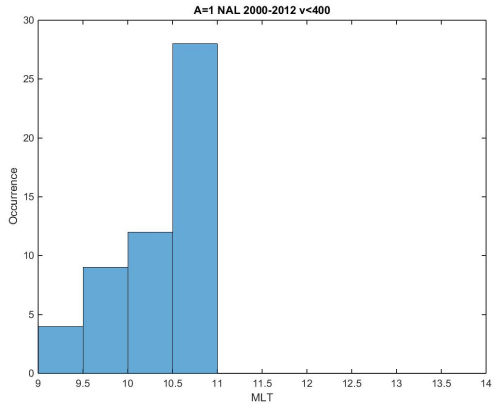

(b) A=1 NAL for both B_z polarities.

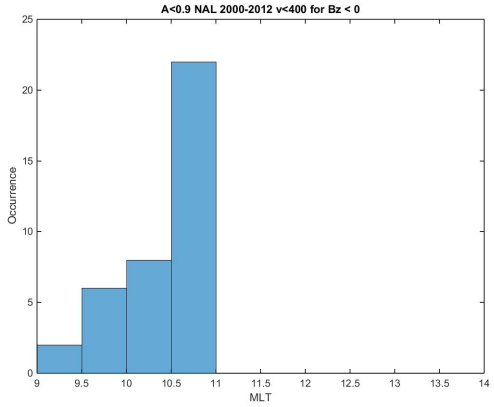

(c) A<0.9 NAL for $B_z < 0$.

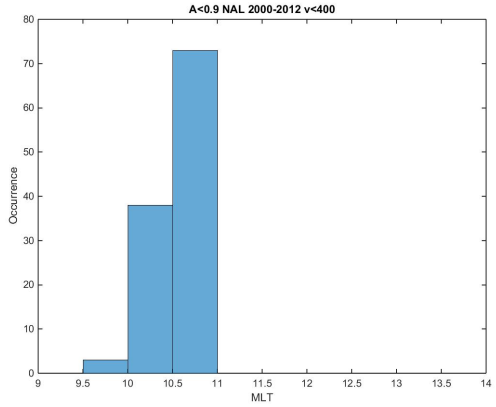

(d) A<0.9 NAL for both B_z polarities.

Figure 5.8: Occurences of arcs and complex structures observed at NAL over MLT when v <400 km/s.

Chapter 6

Discussion

The results presented in the previous chapter are given in terms of arciness indexes (as defined in chapter 4.2) and will, in this chapter, be related to the different dayside auroral forms discussed in chapter 3.3 and summarized in figure 3.2 based on previous studies by Sandholt et al.(2002).
The type 1 cusp aurora has strong enhancements in the green emission line as PMAFs corresponding to medium to high arciness indexes ($0.7 \leq A \leq 1$). The type 2 cusp aurora shows strong emissions of the 557.7 nm line in the pre-and postnoon sectors, also, giving arciness indexes between 0.7 and 1. For this auroral type, the noon sector presents few and weak green auroral forms (thereby named "midday gap" as defined in section 3.3) and will therefore be assigned a weak arciness index between 0.4 and 0.6. The type 3 aurora is observed in the mid-morning (09.00 to 11.00 MLT) with dominating diffuse green structures. The diffuseness of the aurora prohibits auroral structures like arcs and will therefore correspond to low arciness values ($0.4 \leq A \leq 0.6$). Type 4 and type 5 auroras are both dominated by arcs and will therefore be assigned high arciness indexes ranging from 0.7 to 1.

6.1 Distribution of auroral forms for a northward oriented interplanetary magnetic field

Under conditions of northward IMF, $B_z > 0$, reconnection will occur in the high-latitude magnetopause tailward of the cusp, called the tail lobes. Tail lobe reconnection occurs first in one hemisphere and then in the other and due to the high latitude

location, the newly closed field lines will contain plasma of both magnetosheath and magnetospheric origin.

By comparing the results obtained for northward IMF in this study, represented in figures 5.1 and 5.2, with the identifications of auroral types made by Sandholt et al.(1998, 2002) and their corresponding precipitation regions proposed by Newell and Meng (1992), the observations defined by arciness index data will be connected to the different auroral forms.

6.1.1 B_y positive

Events of B_y >0 in the morning sector, here defined for 09.00-10.00 MLT, are typically populated by complex auroral structures (A<0.9) with some presence of arcs (A=1) over Longyearbyen (figures 5.1b and 5.1d respectively). Comparing with auroral forms detected over Ny-Ålesund (figures 5.2b and 5.2d), fewer forms corresponding to complex structures (A<0.9) are observed in the mid-morning sector (09.00-10.30 MLT) and also a higher amount of arcs (A=1) within the same time sector.
The arcs observed over Longyearbyen and Ny-Ålesund correspond to type 4 aurora, known to be multiple arcs from 73 to 77°MLAT. Discrete forms of both green and red emission lines exist for this aurora type, with the northernmost forms typically being red emission lines and are not analyzed in this study since only the green emission line is observed. The high number of arcs (A=1) observed over Ny-Ålesund, when compared to those seen over Longyearbyen from 09.00 to 10.30 MLT might be caused to the movement of the type 2 auroral forms into the prenoon sector.
A high number of complex structures (A<0.9) is observed over both Longyearbyen and Ny-Ålesund in the mid-morning time sector. They are mainly discrete arc-like features within the type 4 aurora (0.7≤A<1). Over Longyearbyen, the type 3 aurora may also be observed between 09.00 and 12.00 MLT. This auroral type is diffuse (0.4≤A≤0.6) and typically located equatorward of the type 4 aurora and may be observed as complex auroral structures (A<0.9).
The auroral forms in the mid-morning/prenoon sector are originating from different precipitation regions: LLBL, BPS and CPS. The type 4 aurora, here observed by arcs (A=1) and complex auroral forms (A<0.9), is originating from the BPS extending over to the dayside from the nightside plasma sheet. The plasma in this region is a mix of magnetosheath and magnetospheric plasma due to the the high-latitude reconnection in the tail lobes. The diffuse type 3 aurora present at lower latitudes

(around 70 to 74°MLAT) arise from the CPS composed of magnetospheric plasma travelling around to the dayside from the nightside.
The midday sector (11.00 to 13.00 MLT) has consistently low occurrences (around 20 to 40 occurrences in each 30 minute bin) of arcs and complex structures at both stations which is the presence of the "midday gap" seen figures 5.1d and 5.2d. By comparing figures 5.2a and 5.2b, the midday gap is less pronounced for B_y >0 than B_y <0. However, the occurrence rates are low throughout that time sector so no concrete conclusions can be made. The characteristic aurora type for this time sector is the type 2 aurora originating from the cusp. This aurora type is calm and has low intensities if steady IMF conditions apply which result in the few observations made in this study and earlier studies [Wang et al., 2010, Sandholt et al., 1998, Dandekar and Pike, 1978]. The aurora will be diffuse of nature with low arciness values (0.4 to 0.6). However, some auroral forms have been observed corresponding to this type and are normally intense green features located in the north-and equatorward boundaries of the cusp indicating that they come from accelerated magnetosheath plasma. Diffuse aurora corresponding to type 3 may also be observed on lower latitudes in this time sector.
The postnoon sector in this study is a brief region confined to the time span between 13.00 and 14.00 MLT. The occurrence of complex structures is low (20 to 30 occurrences in each 30 minute bin), shown in figures 5.1b and figures 5.2b, compared to the occurrence of auroral arcs (up to 90 occurrences in Longyearbyen and 140 in Ny-Ålesund in each 30 minute bin), shown in figures 5.1d and 5.2d, respectively. These arcs (A=1) are the type 5 aurora generally present from 13.00 to 16.00 MLT and are characterized by bright auroral arcs. As the postnoon sector is dominated by the type 5 aurora with high arciness values ($0.8 \leq A \leq 1$), it mainly contains arcs (A=1) and thus the amount of complex structures (A<0.9) will be limited here. The arcs (A=1) tend to concentrate at higher latitudes which might cause the higher number of occurrences in both the Longyearbyen and Ny-Ålesund field of views. These arcs also arise from the dayside extension of the CPS containing magnetospheric plasma due its position near the convection reversal where the plasma will flow sunward on higher latitudes.

6.1.2 B_y negative

When B_y <0, the convection flow will be reversed compared to the one for B_y >0. This will cause some differences in the observed auroral forms.

The mid-morning sector (09.00-10.30 MLT) has more complex structures (A<0.9) observed over Longyearbyen (up to 190 occurrences in the 09.00 to 09.30 MLT bin), as observed in figures 5.1a and 5.2a. More arcs (A=1) are observed over Ny-Ålesund (around 280 occurrences in total) than when B_y >0 which can be seen by comparing figures 5.2c and 5.2d respectively. This might be due to the type 4 aurora (0.7≤A≤1) extending polewards towards noon. The high number of arc (A=1) occurrences in Ny-Ålesund and the high number of complex structure (A<0,9) occurrences in Longyearbyen may be due to auroral structures appearing with different arciness indexes (A=1 in NAL and A<0.9 in LYR) because of their partially overlapping field of views, as discussed in chapter 4.2. The midday sector in this case also contain a very low number of auroral forms consistent with the "midday gap aurora", although some auroral features are observed in this time sector (figures 5.1a, 5.1c, 5.2a and 5.2c) corresponding to the type 2 cusp aurora. The data suggests that the midday gap is more pronounced for B_y <0 than B_y >0 for cases of B_z >0. It could be that under B_y <0 there is more data in the transition zone, between 0.9<A<1 (which is not included in the plots) leading to a lower occurrence rate and a more pronounced midday gap under B_y <0 than for B_y >0.
The extension of the type 2 cusp aurora into the prenoon sector can be observed as complex structures (A<0.9) in the Longyearbyen field of view, making a contribution to the elevated occurrence of complex structures (A<0.9) observed in figure 5.1a. The type 5 aurora is observed with the same signatures as for B_y >0, but with one distinction. The number of arcs observed in Longyearbyen (figure 5.1d) between 13.30 and 1400 MLT is larger and more distinct than that observed in Ny Ålesund for the same IMF conditions (figure 5.2d) which may be due to the cusp aurora moving poleward and westwards instead of into the prenoon sector.

6.2 Distribution of auroral forms for a southward oriented interplanetary magnetic field

For southwards directed IMF (B_z <0), the reconnection point will be located at the nose of the magnetosphere if there is no contribution of the B_y component. The reconnection point will be shifted towards dawn for positive B_y and dusk for negative B_y, changing the geometry of the ionospheric convection cells.
This study focused on cases with high B_z magnitude, confined to the interval between -10 and -5 nT in order to ensure steady IMF conditions of B_z <0 which will keep the

same reconnection mechanism throughout the analysis. Only observations from Ny-Ålesund will be considered as they agree with data from Longyearbyen. By comparing the panels on the left side (B_y <0) of figure 5.3 with ones on the right side (B_y >0), the presence of complex structures (A<0.9) varies in all time sectors of the day between the B_y polarities. The only exception is between 09.30 and 10.30 MLT where the low occurrence is consistent for both polarities. The occurrence of arcs (A=1) between 09.00 and 09.30 MLT is elevated for both polarities. Throughout the rest of the day, B_y <0 has a distribution of arcs (A=1) in the mid-morning sector (here 09.30 to 11.00 MLT) that is not observed for B_y >0. This latter polarity has a presence of arcs in the midday sector (11.00-13.00 MLT) and in the postnoon sector (13.00-14.00 MLT) which is not present when B_y <0. This strongly southwards directed IMF present fewer data points than the -5nT< B_z <-10nT bin which makes identifying the different populations of auroral forms more challenging, especially in the cusp region (midday).
In the same manner as in the previous section, the identifications of auroral types made by Sandholt et al.(1998, 2002) and their corresponding precipitation regions proposed by Newell and Meng (1992) will be compared to the observations defined by arciness index data for Ny-Ålesund, represented in figures 5.3 and 5.4, which then will be connected to the different auroral forms for southward IMF.

6.2.1 B_y positive

For B_y >0, the distribution is dominated by a population of complex structures (A<0.9) and a concentration of auroral arcs (A=1) between 09.00 and 09.30 MLT, as seen in figures 5.3a and 5.3c, respectively. These observed features may correspond to the type 1 aurora and the type 4 aurora originating from two different precipitation regions. The type 4 aurora is typically seen in the morning sector, below 75°MLAT (but still within the field of view of the Ny-Ålesund ASC) and contains single arcs. Also present within this sector is movement of the type 1 cusp aurora. When B_y >0, PMAFs composed of mainly red line aurora are present, but also some green auroral structures moving poleward through the morning sector can be seen. These auroral particles arise from magnetosheath plasma from newly opened field lines. As they are convecting across the polar cap, they deposit solar wind particles, and are therefore a signature of dayside reconnection. Due to the southward oriented B_z component, the mid-morning sector contains a mixture of both type 1 and type 4 auroras.

The midday sector contains few arcs (A=1), but a higher number of complex structures (A<0.9). These complex structures arise essentially from events in 2003 and 2004, which are years of solar maximum, suggesting strong direct coupling, and have medium to high arciness values (0.6-0.9). This large population is only observed when B_z <0 and B_y >0. All observations in this time range correspond to the green emission line within the type 1 aurora which is due to the strong IMF B_z <0 permitting particle precipitation directly into the ionosphere. The complex features (A<0.9) in the type 1 cusp aurora may be corona aurora having medium to high arciness (around 0.8). This type also have corresponding emissions in the 630.0 nm band at around 70 to 75°MLAT.
The postnoon sector (13.00-14.00 MLT) is composed of a few cases of complex structures, but mainly arcs. These arcs correspond to events in 2006 and 2008 and the complex structures to events in 2003, 2006 and 2007. They are related to the type 5 aurora and are originating from the dayside extension of the BPS containing magnetospheric plasma and from the LLBL containing a mix of magnetosheath and magnetospheric plasma.

6.2.2 B_y negative

For B_y <0, the mid-morning sector is mainly composed of a higher number of arcs (A=1) and complex structures (A<0.9) than for B_y >0 from 09.00 to 09.30 MLT. These auroral forms are related to the type 4 aurora originating from the nightside BPS with magnetospheric plasma convecting sunward. The midday sector, normally populated by the green emission band in the type 1 cusp aurora, is nearly empty. One assumption is that for high magnitudes of B_z, the cusp 1 aurora for B_y >0 is mainly composed of red emission line auroral forms which are not taken into account in this analysis. An other explanation may be that the green auroral forms originating from the cusp have already migrated poleward through the postnoon sector. The type 5 aurora is also present postnoon. This study show a very limited number of arcs (A=1) and a higher number complex structures (A<0.9).

6.3 Solar wind velocity effect on dayside auroral forms

The distribution of dayside auroral forms, observed over Longyearbyen, in terms of arcs (A=1) and complex structures (A<1) is similar when increasing the solar wind velocity from 400 km/s to 800 km/s when IMF B_z <0, as observed in figure 5.5. Arcs (A=1) and complex structures (A<1) are present in the mid-morning (09.00-11.00 MLT), midday (11.00-13.00 MLT) and postnoon (13.00-14.00 MLT) sectors. The velocity bins 400< v <500 km/s and 500< v <600 km/s both show a gap in the end of the midday sector, between 12.00 and 13.00 MLT, where no arcs (A=1) and only a few occurrences of auroral structures with medium to high arciness (0.7-0.9) are present. The velocity bin with v <400 km/s, show an arciness distribution concentrated in the mid-morning sector, mainly between 10.00 and 11.00 MLT which will be discussed in further detail. The bin concerning very high solar wind velocities, v >800 km/s, show few data points and will not be discussed further.

By looking at equation 2.18, the solar wind velocity is expected to be partially responsible (together with the solar wind density) for the location of the magnetopause reconnection point and thus, the location of the cusp and the dayside aurora. However, the data show no difference in the time distribution of auroral structures when varying the solar wind velocity. Dimmock et al.(2014) discussed that the amplitude of fluctuations in the dayside magnetosheath increases for solar wind above 400 km/s. This increase in turbulence could lead to enhancements of chaotic aurora, hence complex auroral structures (A<1). Milan et al.(2010) studied the dependence of the brightness of the auroral oval on K_p and solar wind parameters (IMF orientation, solar wind density, velocity and pressure). It was concluded that the the solar wind velocity does not play a significant role in the location and size of the average auroral oval as well as its brightness. The brightness and shape of the oval is related to the direction of the drift around Earth of electrons and ions after being injected into the plasma sheet from nightside reconnection. The location of the oval corresponds to the ionospheric mapping of the field aligned current systems. Therefore, there is no clear correlation between the solar wind velocity and the dayside auroral forms.

However, solar wind velocity below 400 km/s presents an interesting distribution of arcs (A=1) and complex structures (A<0.9) in the mid-morning sector. The histograms for Longyearbyen and Ny-Ålesund, when considering IMF B_z <0 and then all orientations of the IMF in figures 5.7 and 5.8, all show the same trend of few

arcs (A=1) and complex structures (A<0.9). Their occurrence between 09.00 and 09.30 MLT is at a minimum, ranging between 0 and 5. The number of occurrences will rise between 09.30 and 10.30 MLT, except for complex structures (A<0.9) over Longyearbyen when B_z <0 (figure 5.7c). All cases reach a peak in the number of occurrences from 10.30 to 11.00 MLT, between 18 and 90 occurrences.

The arcs (A=1) observed from 09.00 to 10.30 MLT may be related to the type 4 aurora (multiple arcs). By examining the distribution of actual arciness indexes in figure 5.6, clusters of complex structures with medium arciness (A=0.65-0.8) and also arcs (A=1) are observed between 10.30 and 11.00 MLT can be due to enhancements in the green emission line in PMAFs originating from the type 1 cusp aurora as well as the type 2 cusp aurora. Low arciness auroral structures (0.4≤A≤0.6) also occur in this time span and are caused by the type 3 diffuse aurora.

Chapter 7

Conclusions

This study shows that the combination of the arciness index (describing how arc-like an auroral form observed in the field of view of an all-sky camera is) and solar wind data (IMF orientation and magnitude, and solar wind velocity) can be used in order to determine the different characteristic dayside aurora observed between 09.00 and 14.00 MLT. Contrary to most studies done on the dayside aurora phenomena, this analysis gives a general overview of all auroral events between 2000 and 2012.

Looking at dayside structures for IMF B_z polarities separately and comparing each of their corresponding B_y polarities to each other, 5 different types of auroras (defined by Sandholt et al.(2002)) were detected and mapped back to their respective precipitation regions determined by Newell and Meng (1992).

- For IMF B_z >0 and B_y >0, the type 3 (0.4≤A≤0.6) and type 4 (0.7<A≤1) auroras were observed in the mid-morning (09.00-11.00 MLT) sector, as well as the prenoon extension of the type 2 cusp aurora originating from the LLBL, CPS, BPS and the cusp, respectively. The midday sector (11.00-13.00 MLT) is populated by the type 2 cusp aurora (0.4≤A≤0.6). Postnoon (13.00-14.00 MLT), type 5 auroral arcs (0.8<A≤1), originating from the CPS, were observed.
- For IMF B_z >0 and B_y <0, the mid-morning sector is populated by type 4 auroral arcs. The midday sector presents few auroral forms corresponding with the type 2 cusp aurora. This is consistent with the "midday gap" defined by Dandekar and Pike (1978). Postnoon was populated by the type 5 aurora and the postnoon migration of type 2 cusp auroral forms.
- For IMF B_z <0 and B_y >0, type 1 (0.8<A≤1) and type 4 aurora were observed mid-morning. The midday sector showed a unique high population of complex

structures (A<0,9) corresponding to the type 1 aurora. Postnoon, type 5 auroral arcs originating from the dayside extension of the BPS and from the LLBL were seen.

- For IMF B_z <0 and B_y <0, type 4 auroras from BPS plasma convecting towards noon were observed. The midday sector, again, shows a lack of auroral forms consistent with the "midday gap" assuming that the type 1 cusp aurora mainly is composed of red emissions here which will not be observed in these data sets. However, a change in the polarity of the B_y component introduces this population (figures 5.3b and 5.3d). The lack of events around 10.30-12.00 MLT in figure 5.4a and 5.4b regardless of arciness index. This is an interesting fact since a simple change in B_y cannot account for this. The postnoon sector is composed of type 5 aurora along with the postnoon movement of the type 1 aurora.

The solar wind velocity is a contributing factor to the location of the magnetopause reconnection point, but showed no clear correlation to the distribution of auroral forms when varying the strength between v >400 km/s and v <800 km/s. This conclusion concurs with [Milan et al., 2010, Dimmock et al., 2014]. A future task would be to compare the arciness to solar wind density and pressure. Low solar wind velocities, v<400 km/s for all configurations of the IMF, presented a clear trend in arcs (A=1) and complex structures (A<0.9) in the mid-morning sector (09.00-11.00 MLT) suggesting the presence of type 4 auroral arcs, type 3 diffuse aurora as well as type 1 and 2 cusp aurora (not simultaneously).

The arciness index makes it possible to conveniently conduct studies based on large data sets without needing to examine every image and also prevents the human bias. Arcs are easily observed and related to a specific auroral type where they occur. Complex structures can be everything from coronas to patchy auroras and the same arciness value can correspond to totally different auroral forms. The evolution of auroral structures is also challenging to observe in terms of arciness index,

References

S.-I. Akasofu. A study of auroral displays photographed from the dmsp-2 satellite and from the alaska meridian chain of stations. *Space Science Reviews*, 1974.

S.-I. Akasofu. Interplanetary energy flux associated with magnetospheric substorms. *Planetary Space Science*, 1979.

H. Alfvén. Existence of electromagnetic-hydrodynamic waves. *Nature*, 1942.

N. Balan, R. Skoug, S. Tulasi Ram, P. K. Rajesh, K. Shiokowa, Y. Otsuka, I. S. Batista, Y. Ebihara, and T. Nakamura. Cme front and severe space weather. *Journal of Geophysical Reserch: Space Physics*, 2014.

W. Baumjohann and R.A. Treumann. *Basic Space Plasma Physics*. Imperial College Press, London, 1996.

A. Brekke. *Physics of the Upper Polar Atmosphere, Second Edition*. Springer, 2013.

P.A. Cassak and M.A. Shay. Scaling of asymmetric magnetic reconnection: General theory and collisional simulations. *Physics of Plasmas*, 2007.

Francis Chen. *Introduction to plasma physics and controlled fusion*. Plenum Press, New York, 1984.

G. Chisham, M.P. Freeman, I.J. Coleman, M. Pinnock, M.R. Hairston, M. Lester, and G. Sofko. Measuring the dayside reconnection rate during an interval of due northward interplanetary magnetic field. *Annales Geophysicae*, 2004.

S.W.H. Cowley. Excitation of flow in the earths magnetosphere-ionosphere system: Observations by incoherent scatter radar. *Polar Cap Boundary Phenomena*, 1998.

S.W.H. Cowley. Magnetosphere-ionosphere interactions: A tutorial review. *American Geophysical Union*, 2000.

J.A. Cumnock, R.A. Heelis, M.R Hairston, and P.T. Newell. High-latitude ionospheric convection pattern during steady northward interplanetary magnetic field. *Journal of Geophysical Research*, 1995.

B.S. Dandekar and C.P. Pike. The midday discrete auroral gap. *Journal of Geophysical Research*, 1978.

A.P. Dimmock, K. Nykyri, and T.I. Pulkkinen. A statistical study of magnetic field fluctuations in the dayside magnetosheath and their dependence on upstream solar wind conditions. *Journal of Geophysical Research: Space Physics*, 2014.

J.W. Dungey. Interplanetary magnetic field and the auroral zones. *American Physical Society*, 1961.

J.W. Dungey. *The structure of the exosphere, or adventures in velocity space, in Geophysics: The Earths Environment, edited by C. DeWitt, J. Hiebolt and A. Lebeau, 526-536.* Gordon and Breach, New York, 1963.

E.Parker. Extension of the solar corona into interplanetary space. *Journal of Geophysical Research*, 1959.

W.C. Feldman. Unresolved questions about the structure and dynamics of the extended solar corona. *American Geophysical Union*, 1999.

Y.I. Feldstein and G.V. Starkov. Dynamics of auroral belt and polar geomagnetic disturbances. *Planetary Space Science*, 1967.

FMI. Miracle. URL `www.space.fmi.fi/MIRACLE/index.html`.

J.T. Gosling and V.J. Pizzo. Formation and evolution of corotating interaction regions and their three dimensional structure. *Space Science Reviews*, 1999.

T.J. Hallinan and T.N. Davis. Small-scale auroral arc distortions. *Planetary Space Science*, 1970.

S.B. Howell. *Handbook of CCD Astronomy.* Cambridge University Press, Second edition, 2006.

M.G. Kivelson and C.T. Russel. *Introduction to Space Physics.* Cambridge University Press, 1995.

R.P. Lepping, D.B. Berdichevsky, L.F. Burlaga, A.J. Lazarusand J. Kasper, M.D. Desch, C.-C. Wuand D.V. Reamesand H.J. Singer, and C.W. Smithand K.L. Ackerson. The bastille day magnetic clouds and upstream shocks: Near-earth interplanetary observations. *Solar Physics*, 2001.

R.P. Lepping, D.B. Berdichevsky, and C.-C. Wu. Sun-earth electrodynamics: The solar wind connection. *Recent Res. Devel. Astrophys.*, 2003.

A.T.Y. Lui and C.T. Anger. A uniform belt of diffuse auroral emission seen by the isis-2 scanning photometer. *Planetary Space Science*, 1973.

R.L. McPherron. Magnetospheric substorms. *Rev. Geophys. Space Phys.*, 1979.

S.E. Milan, T.A. Evans, and B. Hubert. Average auroral configuration parameterized by geomagnetic activity and solar wind conditions. *Annales Geophysicae*, 2010.

J. Moen, P.E. Sandholt, M. Lockwood, A. Egeland, and K. Fukui. Multiple, discrete arcs on sunward convecting field lines in the 14-15 mlt region. *Journal of Geophysical Research*, 1994.

NASA. Advanced composition explorer (ace). URL `www.nasa.gov/directorates/heo/scan/services/missions/solarsystem/ACE.html`.

P.T. Newell and C.I. Meng. Mapping the dayside ionosphere to the magnetosphere according to particle precipitation characteristics. *Geophysical Research Letters*, 1992.

P.T. Newell, W. Burke, C.I. Meng, E.R. Sanchez, and M.E. Greenspan. Identification and observations of the plasma mantle at low altitude. *Journal of Geophysical Research*, 1991.

T.G. Onsager, J.D. Scudder, M. Lockwood, and C.T. Russell. Reconnection at the high-latitude magnetopause during northward interplanetary magnetic field condition. *Journal of Geophysical Research*, 2001.

N. Partamies, D. Whiter, M. Syrjäsuo, and K. Kauristie. Solar cycle and diurnal dependence of auroral structures. *Journal of Geophysical Research: Space Physics*, 2014.

N. Partamies, L. Juusola, D. Whiter, and K. Kauristie. Substorm evolution of auroral structures. *Journal of Geophysical Research: Space Physics*, 2015.

G.W. Prölss. *Physics of the Earths Space Environment*. Springer, 2004.

Hans Pécseli. *Waves and Oscillations in Plasmas*. CRC Press, 2013.

G. Rostocker, S.-I. Akasofu, R.A. Greenwald, Y. Kamide, K. Kawasaki, A.T.Y. Lui, R.L. McPherron, and C.T. Russel. Magnetospheric substorms-definition and signatures. *Journal of Geophysical Research*, 1980.

C.T. Russell, R.C. Snare, J.D. Means, D. Pierce, D. Dearborn, M. Larson, G. Barr, and G. Le. The ggs/polar magnetic fields investigation. *Space Science Reviews*, 1995.

P.E. Sandholt, B. Jacobsen, B. Lybekk A. Egeland, T.Sten, C.I. Meng, P.T. Newell, F.J. Rich, and E.J. Weber. Structure and dynamics of the polar cleft: Coordinated satellite and ground-based observations in the prenoon sector. *Journal of Geophysical Research*, 1989.

P.E. Sandholt, C.J. Farrugia, J. Moen, Ø. Noraberg, B. Lybekk, T.Sten, and T.Hansen. A classification of dayside auroral forms and activities as a function of interplanetary magnetic field orientation. *Journal of Geophysical Research*, 1998.

P.E. Sandholt, H.C. Carlson, and A. Egeland. *Dayside and Polar Cap Aurora*. Kluwer Academic Publishers, 2002.

E.J. Smith. The heliospheric current sheet. *Journal of Geophysical Research*, 2001.

D.J. Strickland, J.R. Jasperse, and J.A. Whalen. Dependence of auroral fuv emissions on the incident electron spectrum and neutral atmosphere. *Journal of Geophysical Research*, 1983.

M. Syrjäsuo. All-sky camera. Master's thesis, Helsinki University of Technology, Helsinki, Finland, 1996.

M. Syrjäsuo. *Auroral monitoring network: From all-sky camera system to automated image analysis*. PhD thesis, Helsinki University of Technology, Finnish Meteorological Institute Contributions, Helsinki, Finland, 2001.

Q. Wang, J. Liang, Z.J. Hu, H.H. Hu, H. Zhao, H.Q. Hu, X. Gao, and H. Yang. Spatial texture based automatic classification of dayside aurora in all-sky images. *Journal of Atmospheric and Solar-Terrestrial Physics*, 2010.

M. Øieroset, P.E. Sandholt, W.F. Denig, and S.W.H. Cowley. Northward interplanetary magnetic field cusp aurora and high-latitude magnetopause reconnection. *Journal of Geophysical Research*, 1997.

Norges miljø- og biovitenskapelig universitet
Noregs miljø- og biovitskapelege universitet
Norwegian University of Life Sciences

Postboks 5003
NO-1432 Ås
Norway